
Masters Theses

Student Theses and Dissertations

Fall 2011

Mesh optimization of finite element models of wellbore stress analysis

Ming-Yen Lee

Follow this and additional works at: https://scholarsmine.mst.edu/masters_theses



Part of the [Petroleum Engineering Commons](#)

Department:

Recommended Citation

Lee, Ming-Yen, "Mesh optimization of finite element models of wellbore stress analysis" (2011). *Masters Theses*. 4138.

https://scholarsmine.mst.edu/masters_theses/4138

This thesis is brought to you by Scholars' Mine, a service of the Missouri S&T Library and Learning Resources. This work is protected by U. S. Copyright Law. Unauthorized use including reproduction for redistribution requires the permission of the copyright holder. For more information, please contact scholarsmine@mst.edu.

MESH OPTIMIZATION OF FINITE ELEMENT MODELS
OF WELLBORE STRESS ANALYSIS

by

MING-YEN LEE

A THESIS

Presented to the Faculty of the Graduate School of the
MISSOURI UNIVERSITY OF SCIENCE AND TECHNOLOGY

In Partial Fulfillment of the Requirements for the Degree

MASTER OF SCIENCE IN PETROLEUM ENGINEERING

2011

Approved by

Andreas Eckert, Advisor
Runar Nygaard, Co-Advisor
Ralph E. Flori, Jr.

© 2011

Ming-Yen Lee

All Rights Reserved

ABSTRACT

Numerical modeling methods such as the widely used finite element method provide an excellent opportunity to analyze the wellbore state of stress for a variety of applications such as wellbore integrity, wellbore design or hydraulic fracturing. However, numerical modeling methods introduce errors by nature and may not precisely match the analytical solution if the meshing of the numerical model is not carefully taken care of. This study presents a parametric study of the meshing parameters mesh density, element type, and model size for 2-dimensional and 3-dimensional vertical wellbore models under three different types of boundary conditions, and a guideline for mesh optimization is provided. The implications of the accuracy of numerical modeling results are shown by calculating the safe mud weight window for different stress regimes for a non-optimized wellbore mesh and an optimized mesh. Utilizing a non-optimized mesh for wellbore stress analysis may lead to a significant misinterpretation of the minimum usable mud weight and borehole collapse may result. Exemplary cases of wellbore stability during drilling and wellbore integrity of CO₂ sequestration in a generic anticline structure have been studied with the optimized 3-D wellbore model.

ACKNOWLEDGMENTS

I would like to express my gratitude to my advisor, Dr. Andreas Eckert, for his guidance and support during my graduate studies. His technical and editorial advice was essential to the completion of this thesis and has taught me invaluable insights and lessons on the workings of academic research in general. And because of him, I greatly refined my taste in beer.

My thanks also go to the co-advisor, Dr. Runar Nygaard, for providing not only many academic comments but also industrial experiences that improve the contents of this thesis.

Dr. Ralph E. Flori Jr., the Chair of the Geological Sciences and Engineering Department with numerous teaching awards, deserves a special thanks as my thesis committee member.

I am also grateful to my friends Saeed Salehi, Amin Amirlatifi, Imowo Akpan, and Matthew Paradeis with whom I worked together in the office at the Rock Mechanics Center for helping me considerably by sharing their knowledges and opinions. In particular, I reference some of their works in my thesis: Amin implemented the coupling module of the geomechanical and reservoir simulation, and Matt performed the modeling of the generic reservoir.

Lastly, I would like to thank and dedicate this thesis to my family who made this possible: my wife Ying-Chien for her understanding, love, and encouragement during the past few years; my children Karina, Andrew, Ryan, and the coming baby Jeremy for bringing me happiness and joy; my parents I-Hsien and Li-Ching for their love and care throughout my life.

TABLE OF CONTENTS

	Page
ABSTRACT.....	iii
ACKNOWLEDGMENTS	iv
LIST OF ILLUSTRATIONS.....	viii
LIST OF TABLES.....	x
SECTION	
1. INTRODUCTION.....	1
1.1. PREVIOUS STUDIES OF FINITE ELEMENT ANALYSIS FOR BOREHOLE STRESS	1
1.2. STUDY OBJECTIVES	2
2. THEORETICAL BACKGROUND	3
2.1. BASIC THEORY OF STRESS.....	3
2.1.1. Stress at a Point	3
2.1.2. Traction Vector.....	4
2.1.3. Principal Stresses.....	6
2.1.4. Mean Stress and Deviatoric Stress	6
2.1.5. Andersonian Stress Regime.....	7
2.2. STRESS AROUND A WELLBORE	7
2.3. ROCK FAILURE CRITERIONS	9
2.3.1. Compressive Failure.....	9
2.3.2. Tensile Failure	11
2.4. EFFECT OF PORE PRESSURE AND MUD PRESSURE TO FORMATION FAILURE	12
2.5. SAFE MUD WEIGHT WINDOW.....	13
2.6. FINITE ELEMENT ANALYSIS.....	14
2.6.1. Governing Equation in Finite Element Modeling	14
2.6.2. Finite Element Method.....	15
2.6.3. Error Source and Approximation	16
3. GEOMECHANICAL MODEL AND MODELING APPROACH.....	19
3.1. MODEL SETTINGS.....	19

3.2. MAPPED MESHING APPROACH	21
3.3. MODEL INPUT AND BOUNDARY CONDITIONS	21
3.4. PARAMETRIC STUDY	23
4. RESULTS.....	24
4.1. 2-D WELLBORE MODEL USING DISPLACEMENT BOUNDARY CONDITIONS.....	24
4.1.1. Comparison of the Base Model Results to the Analytical Solution.....	24
4.1.2. Sensitivity Analysis of Model Size	26
4.1.3. Sensitivity Analysis of Element Type	29
4.1.4. Sensitivity Analysis of Mesh Density	30
4.1.5. General Meshing Guideline.....	32
4.2. OPTIMIZATION OF 2-D WELLBORE MODEL	33
4.3. 2-D WELLBORE MODEL USING STRESS BOUNDARY CONDITIONS AND DRILLING SIMULATION BOUNDARY CONDITIONS.....	34
4.4. 3-D WELLBORE MODEL BUILT BASED ON 2-D WELLBORE MODEL.....	37
4.4.1. Comparison of the 3-D Base Model Results to the 2-D Base Model and the Analytical Solution	37
4.4.2. Sensitivity Analysis of Model Height and Element Height	38
4.4.3. Sensitivity Analysis of Element Type	38
4.4.4. Optimized 3-D Wellbore Model.....	39
5. DISCUSSION	40
5.1. 2-D MODELS USING DISPLACEMENT BOUNDARY CONDITIONS.....	40
5.2. COMPARISON OF MODELS USING DIFFERENT BOUNDARY CONDITIONS.....	42
5.3. UTILIZATION OF 3-D MODELS.....	42
5.4. IMPLICATIONS OF SAFE MUD WEIGHT PREDICTION	43
5.5. APPLICATION OF THE WELLBORE MODEL ON GEOLOGICAL STORAGE OF CO ₂ IN A GENERIC RESERVOIR	45
5.5.1. Geomechanical Modeling for Carbon Storage	45
5.5.2. Reservoir-Scale Model and Wellbore-Scale Model.....	46
5.5.3. Wellbore Stability of a Vertical Well in the Reservoir Layer	47

5.5.4. Wellbore Stability of Inclined Well in the Reservoir Layer	56
5.5.5. CO ₂ Sequestration Model.....	60
5.5.6. Wellbore Integrity after CO ₂ Injection.....	60
5.6. OUTLOOK.....	62
6. CONCLUSIONS	64
APPENDIX.....	67
BIBLIOGRAPHY.....	68
VITA	72

LIST OF ILLUSTRATIONS

Figure	Page
2.1. Stress components in three dimensions.....	4
2.2. Traction vectors acting on a plane with normal unit vector \hat{n}	5
2.3. The effective stresses in cylindrical coordinate system and failure types around the borehole	9
2.4. Mohr circle diagram showing compressive failure as the Mohr Circle touches the Mohr-Coulomb failure envelope.....	11
2.5. Influence of pore pressure toward formation failure.....	12
2.6. Influence of mud pressure toward formation failure.....	12
2.7. Process for FE simulation of physical problem.....	17
2.8. A schematic view showing the analytical solution of the continuum and the numerical solution of the two discrete systems.....	18
3.1. The 2-D base model using a mapped meshing approach and varied mesh densities in the sub-regions	20
3.2. The 3-D base model generated from the 2-D cross-section	20
3.3. Three types of boundary conditions: (a) displacement; (b) stress; (c) drilling process simulation	22
4.1. S11 distribution in the 2-D wellbore model	25
4.2. The modeled results from the base model as compared to the analytical solution	25
4.3. Influence of model size on the effective stresses at: (a) $\sigma_{\theta\theta}$ at 0° , (b) σ_{rr} at 0° , (c) $\sigma_{\theta\theta}$ at 90° and (d) σ_{rr} at 90°	27
4.4. Influence of element type for the hoop stress at 90°	30
4.5. Influence of the radial mesh density in the near-wellbore region for the hoop stress at 90°	32
4.6. The modeled results from the optimized 2-D model compared to the analytical solutions	34
4.7. Hoop stress at 0° showing a great discrepancy near the far-field for the base model under the stress boundary condition.....	36
4.8. Base model using three boundary conditions and compared to the analytical solutions.....	36
4.9. 2-D and 3-D Base models using displacement boundary conditions with comparison to the analytical solutions	37

5.1.	Stresses at the element integration points extrapolated to the nodal positions introducing greater errors, especially near the borehole wall	41
5.2.	Reservoir model of anticline for CO ₂ storage	46
5.3.	Mud weight windows of the reservoir layer of vertical well at (a) crest, (b) limb, and (c) syncline under the extensional stress regime	50
5.4.	Mud weight windows for the reservoir layer of vertical wells at (a) crest, (b) limb, and (c) syncline under the strike-slip stress regime	51
5.5.	Mud weight windows of vertical wells at (a) crest, (b) limb, and (c) syncline under the compressional stress regime.....	52
5.6.	Mud weight window of the vertical well at the crest of the anticline under the compressional stress regime	53
5.7.	Mud weight window of the vertical well at the crest of the anticline for the total depth under the extensional stress regime.....	53
5.8.	Reservoir models of coefficient of friction 0.05 under (a) extensional stress regime and (b) compressional stress regimes.....	54
5.9.	Reservoir models of coefficient of friction 0.80 under (a) extensional stress regime and (b) compressional stress regimes.....	55
5.10.	Mud weight windows of a 45°-inclined well (with respect to σ_1) at (a) crest, (b) limb, and (c) syncline of the reservoir layer under the strike-slip stress regime	57
5.11.	Mud weight windows of 45°-inclined well at (a) crest, (b) limb, and (c) syncline of the reservoir layer under the compressional stress regime.....	58
5.12.	Mud weight windows of horizontal well at crest of the reservoir layer under (a) extensional, (b) strike-slip, and (c) compressional stress regimes.....	59
5.13.	Collapse pressure and breakdown pressure due to CO ₂ injection of the vertical well in the extensional case at day 1	61
5.14.	Collapse pressure and breakdown pressure due to CO ₂ injection of the vertical well in the extensional case after 25 years	62
5.15.	Evaluation of optimal wellbore path based on (a) locations of the anticline, and (b) wellbore trajectories.....	63

LIST OF TABLES

Table	Page
4.1. Errors of the effective stresses at borehole wall for the 2-D base model	24
4.2. Sensitivity analysis of the model size using displacement boundary conditions ...	29
4.3. Sensitivity analysis of the model size using displacement boundary conditions ...	29
4.4. Sensitivity analysis of the mesh density around the borehole circumference using displacement boundary conditions	31
4.5. Sensitivity analysis of the mesh density along the radial distance in the near-wellbore region using displacement boundary conditions	31
4.6. Errors of the modeled results from the optimized 2-D model compared to the base model	33
4.7. Errors at the wellbore surface for the base model and the optimized model under the three types of boundary conditions	35
4.8. 2-D and 3-D model results compared to analytical solutions	38
4.9. Sensitivity analysis of the model height for the 3-D model	38
4.10. Sensitivity analysis of the element height for the 3-D model.	38
4.11. Sensitivity analysis of the element type for the 3-D model	39
4.12. 3-D and 2-D optimized model results compared to the analytical solutions.....	39
5.1. State of stress for the different stress regimes applied to the wellbore models.....	43
5.2. Stress errors at the borehole wall of the base model and optimized model under the three stress regimes	44
5.3. Predicted safe mud weight window using the Mohr Coulomb failure criterion	44
A1. Model settings of the reservoir model	67

1. INTRODUCTION

1.1. PREVIOUS STUDIES OF FINITE ELEMENT ANALYSIS FOR BOREHOLE STRESS

The analytical solution of the borehole stresses for a linear elastic material is given by the well-known solution derived by Ernst Gustav Kirsch [1] in 1898. Bradley [2] and Zhang [3] further derived the effective wellbore stresses at the borehole wall for an inclined borehole including pore pressure and mud pressure. However, the analytical solution has limitations in handling complex formation geometry, material heterogeneities and different rheological models.

As computers and commercial numerical software applications have become readily available as a standard engineering tool, a variety of borehole stress studies utilize 2D and 3D finite element analysis for solving geomechanical problems associated with borehole failure [4, 5, 6, 7]. It should be noted that numerical modeling methods introduce errors by nature, as they represent an approximation approach [8], and often utilize assumptions and simplifications for the practical problems. Thus, a common problem of numerical studies is the validation and calibration to analytical solutions and field data. Since this standard modeling procedure is sometimes not available, care has to be taken with numerical codes to provide an accurate solution before the results can be relied on for interpretation.

For wellbore stress analyses, the accuracy of numerical modeling results becomes crucial especially at the wellbore wall where the state of stress changes rapidly. Therefore, a high quality mesh, in addition to a constitutive material behavior and an appropriate way to apply boundary conditions, is required to obtain accurate results. The optimization of the model mesh may not be done in every study [9, 10], and to date only few studies have focused on the significant influence by the mesh quality to the numerical modeling results in geomechanical applications [11, 12, 13]. Grabinsky et al. [11] studied the impact of different element types to provide good quality discretizations for rock excavation for tunnels. Turon et al. [12] showed that results are sensitive to the element size when handling pore cohesive elements in the wellbore fracture zone, and a mesh size as small as 0.5mm in length is necessary to obtain converging solutions. Nipp

and McNulty [13] demonstrated how boundary conditions and element size can affect the accuracy of solutions involving creep around a single borehole in an infinite medium. In summary, these studies support the inference that the discretization parameters of element size, element type, model size and boundary conditions are crucial regarding the accuracy of numerical results. However the majority of numerical wellbore modeling studies rarely consider these influences and an inherent need for an optimization procedure becomes evident. This becomes most crucial when considering wellbore stability scenarios where the mud window is very small.

1.2. STUDY OBJECTIVES

In the present study, the objective is to:

- (1) present a parametric study of mesh parameters with comparison to Kirsch's analytical solution;
- (2) provide a general guideline for optimization of 2-D and 3-D wellbore models to minimize the numerical errors; and
- (3) apply the non-optimized and optimized numerical borehole model in an exemplary wellbore stability analysis and discuss the significance of the numerical errors.

For the wellbore models, a parametric study of the discretization (i.e. mesh) is based on the model size, element size, element type and the application of different types of boundary conditions. The numerical results around the wellbore are to be compared and validated with the analytical solution. An optimizing procedure is to be developed to minimize the numerical errors according to the parametric study. For the case of an exemplary wellbore stability analysis, i.e. the calculation of the safe mud weight window for three different stress regimes, this study is to show the influence of the meshes to the error of the numerical solution and the subsequent analysis of wellbore integrity. Optimal well placement and CO₂ injection for a generic anticline reservoir on wellbore integrity is further studied.

2. THEORETICAL BACKGROUND

2.1. BASIC THEORY OF STRESS

2.1.1. Stress at a Point. The following Chapter 2.1 summarizes brief stress theory with reference to standard text books [14, 15, 16, 17]. Forces acting on a continuous medium can be categorized into two types: body forces and surface forces. The body forces act throughout the volume of the continuous medium and their magnitudes are proportional to the mass involved (e.g. gravity). In contrast, surface forces act on arbitrary surfaces of the medium. Surface forces can be resolved into two components, one acting normal to the surface, and one acting parallel to the surface. For a continuous medium which is loaded with a uniformly distributed normal force F over a cross-section area A , stress can be defined as:

$$\sigma = \frac{F}{A} \quad (1)$$

To define the stresses at a point in the body, an infinitesimal cube with surfaces oriented in three orthogonal directions is assumed (Figure 2.1). Each surface has a normal stress and two shear stresses acting on it. Considering a surface normal to the x direction, i.e., the x-plane), the normal stress is designated by σ_{xx} . The first subscript denotes the x-plane that the stress is acting on, and the second subscript denotes the direction of the stress. Similarly, σ_{xy} and σ_{xz} represent the shear stress on the x-plane in the y direction and z direction, respectively. Thus, there is a total of nine stress components for a complete description of state of stress at a point, represented by the stress tensor σ_{ij} :

$$\sigma_{ij} = \begin{bmatrix} \sigma_{xx} & \sigma_{xy} & \sigma_{xz} \\ \sigma_{yx} & \sigma_{yy} & \sigma_{yz} \\ \sigma_{zx} & \sigma_{zy} & \sigma_{zz} \end{bmatrix} \quad (2)$$

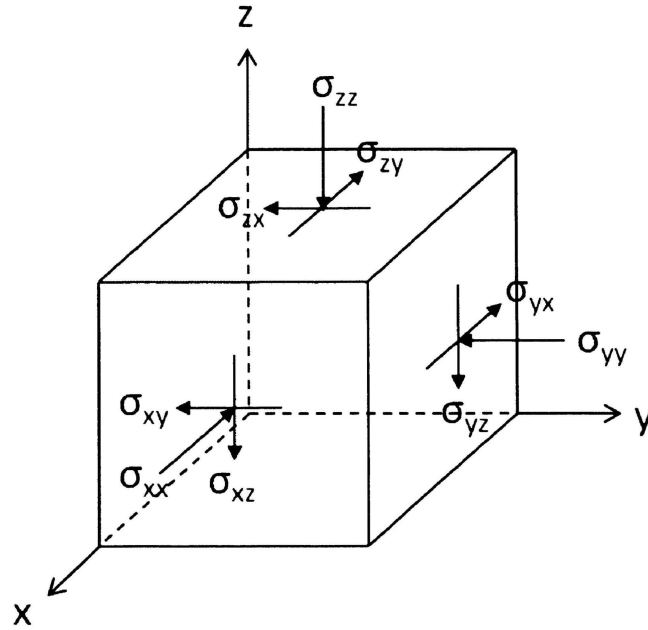


Figure 2.1. Stress components in three dimensions.

Since forces and moments are in equilibrium throughout the body, no rotational movement can be found at any point such that:

$$\sigma_{ij} = \sigma_{ji} \quad (3)$$

Thus, the six shear stress components can be simplified as three independent stress components.

2.1.2. Traction Vector. For an expression of stress on a plane in vector form, the traction vector \vec{T} represents a vector quantity of stress that acts at a point of a surface of arbitrary orientation specified by the unit normal vector \vec{n} on the body. The state of stress at a point in the body is defined by all the traction vectors $\vec{T}(\vec{n})$ on a plane that pass through the point:

$$\vec{T}(\vec{n}) = \lim_{dA \rightarrow 0} \frac{d\vec{F}}{dA} \quad (4)$$

From the force equilibrium in the Cauchy tetrahedron (Figure 2.2), the stress vector $\vec{T}(\vec{n})$ at any point in a continuum medium associated with a plane with normal unit vector \hat{n} can be expressed as a function of \hat{n} :

$$\vec{T}(\vec{n}) = \sigma_{ij} \hat{n}_j \quad (5)$$

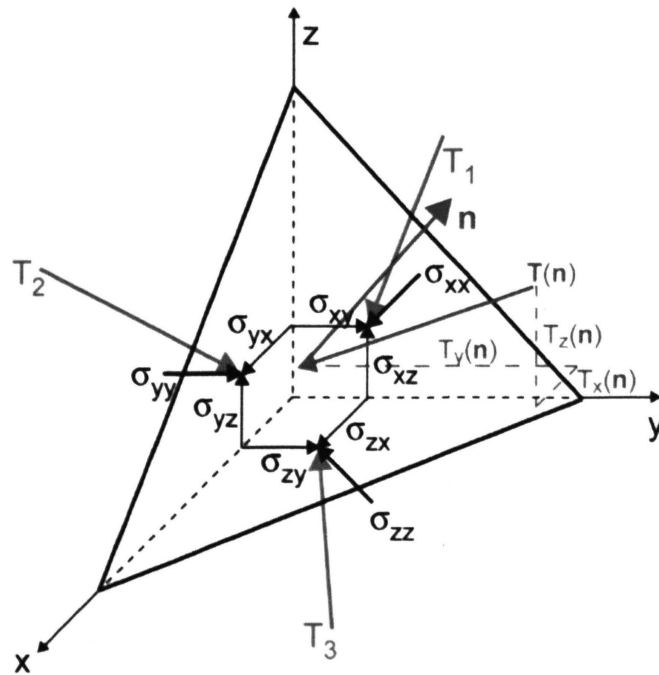


Figure 2.2. Traction vectors acting on a plane with normal unit vector \hat{n} [14].

The equation shows that the stress vector on any arbitrary plane passing through that point can be determined by merely knowing the state of stress at that point.

2.1.3. Principal Stresses. The stress tensor involves six independent stress components, i.e. three normal stresses and three shear stresses, and is dependent on the coordinate system of the imaginary infinitesimal cube. Through coordinate transformation equations for stresses, the stress tensor for any coordinate system can be obtained. In a specific coordinate system where all the shear stresses are zero and only normal stresses exist, the normal stresses are referred to as principal stresses σ_1 , σ_2 , and σ_3 . The stress tensor for the principal stresses can be expressed as:

$$\sigma^p = \begin{bmatrix} \sigma_1 & 0 & 0 \\ 0 & \sigma_2 & 0 \\ 0 & 0 & \sigma_3 \end{bmatrix} \quad (6)$$

2.1.4. Mean Stress and Deviatoric Stress. The deformation of rock corresponding to the stresses involves two types of change: changes in volume and shape. The volume change is determined by the mean stress σ_m , simply given by the arithmetic average of the three principal stresses:

$$\sigma_m = \frac{\sigma_1 + \sigma_2 + \sigma_3}{3} \quad (7)$$

The shape change or distortion is associated to the deviatoric stress. The deviatoric stress σ'_{ij} is defined by subtracting mean stress from the normal stress components:

$$\sigma'_{ij} = \begin{bmatrix} \sigma_{xx} - \sigma_m & \sigma_{xy} & \sigma_{xz} \\ \sigma_{yx} & \sigma_{yy} - \sigma_m & \sigma_{yz} \\ \sigma_{zx} & \sigma_{zy} & \sigma_{zz} - \sigma_m \end{bmatrix} \quad (8)$$

2.1.5. Andersonian Stress Regime. The state of stress in the Earth's crust is commonly referred to as an Andersonian state of stress in which one principal stress is the vertical stress and the other two are the horizontal stresses. Based on the relation of the magnitudes three Andersonian stress regimes can be defined: (1) extensional stress regime, in which σ_1 is the vertical stress; (2) strike-slip stress regime, in which σ_2 is the vertical stress; (3) compressional stress regime, in which σ_3 is the vertical stress.

2.2. STRESS AROUND A WELLBORE

Wellbore instability and thus wellbore failure are directly dependent on the state of stress around the wellbore. Therefore a fundamental understanding of the wellbore state of stress is crucial and has been studied extensively.

Subsurface formations are subject to three in-situ principal stresses σ_1 , σ_2 , and σ_3 , and the state of stress of the rock is initially in equilibrium. When the borehole rock is removed, e.g. during drilling, the acting loads are to be compensated in the adjacent rock around the borehole by redistributing the stresses. After the redistribution of the stresses, local stress concentrations occur in the close vicinity of the wellbore. The linear elastic solution describing the radial and tangential stresses around a circular borehole was first derived by Kirsch [1] in 1898, in which the axis of the hole opening coincides with one axis of the principal stresses. The Kirsch solution is extended by Zhang et al. [3] to take into account the pore pressure and the fluid pressure in the wellbore. For an Andersonian state of stress that σ_1 , σ_2 , and σ_3 are the vertical stress and two far field horizontal stresses [17] and assuming a constant pore pressure and a Biot's coefficient of 1, the effective stresses around the borehole for a vertical well can be obtained [3]:

$$\sigma'_{rr} = \frac{(\sigma_H + \sigma_h - 2P_p)}{2} \left(1 - \frac{R_w^2}{r^2}\right) - \frac{(\sigma_H - \sigma_h)}{2} \left(1 - \frac{4R_w^2}{r^2} + \frac{3R_w^4}{r^4}\right) \cos 2\theta + (P_m - P_p) \frac{R_w^2}{r^2} \quad (9)$$

$$\sigma'_{\theta\theta} = \frac{(\sigma_H + \sigma_h - 2P_p)}{2} \left(1 + \frac{R_w^2}{r^2}\right) - \frac{(\sigma_H - \sigma_h)}{2} \left(1 + \frac{3R_w^4}{r^4}\right) \cos 2\theta - (P_m - P_p) \frac{R_w^2}{r^2} \quad (10)$$

$$\sigma'_z = \sigma_v - P_p - \nu \frac{2R_w^2}{r^2} (\sigma_H - \sigma_h) \cos 2\theta \quad (11)$$

$$\tau'_{r\theta} = -\frac{(\sigma_H - \sigma_h)}{2} \left(1 + \frac{2R_w^2}{r^2} - \frac{3R_w^4}{r^4} \right) \sin 2\theta \quad (12)$$

where σ'_{rr} , $\sigma'_{\theta\theta}$, σ'_z and $\tau'_{r\theta}$ are the radial stress, hoop stress, vertical stress, and shear stress in the r - θ plane, respectively; σ_H , σ_h , and σ_v are the maximum horizontal, minimum horizontal, and the overburden stress, respectively; R_w is the wellbore radius, and r is the distance from wellbore center; θ is the angle with respect to the direction of σ_H ; ν is the Poisson's ratio.

Then the effective stresses at the borehole wall ($r = R_w$) can be written as:

$$\sigma'_{rr} = P_m - P_p \quad (13)$$

$$\sigma'_{\theta\theta} = \sigma_H + \sigma_h - P_m - P_p - 2(\sigma_H - \sigma_h) \cos 2\theta \quad (14)$$

$$\sigma'_z = \sigma_v - P_p - 2\nu(\sigma_H - \sigma_h) \cos 2\theta \quad (15)$$

For the stresses at the wellbore wall, at $\theta = 90^\circ/270^\circ$, the hoop stress reaches its maximum and thus compressive failure or borehole breakouts may occur if the state of stress exceed the compressive strength of the rock (Figure 2.1). The hoop stress is minimum at $r = R_w$ at $\theta = 0^\circ/180^\circ$, and when the hoop stress is in tensile and reaches the tensile strength of the rock, tensile failure occurs (Figure 2.1).

The maximum hoop stress occurs in the direction of the minimum horizontal stress ($\theta = 90^\circ$), and the hoop stress at the borehole wall is given by:

$$\sigma'_{\theta\theta} = 3\sigma_h - \sigma_H - P_p - P_m \quad (16)$$

The minimum hoop stress occurs in the direction of maximum horizontal stress ($\theta = 0^\circ$), and the hoop stress at the borehole wall is given by:

$$\sigma'_{\theta\theta} = 3\sigma_H - \sigma_h - P_p - P_m \quad (17)$$

The radial stress at the borehole wall is given by the difference of fluid pressure and pore pressure, regardless of the angle θ :

$$\sigma'_{rr} = P_m - P_p \quad (18)$$

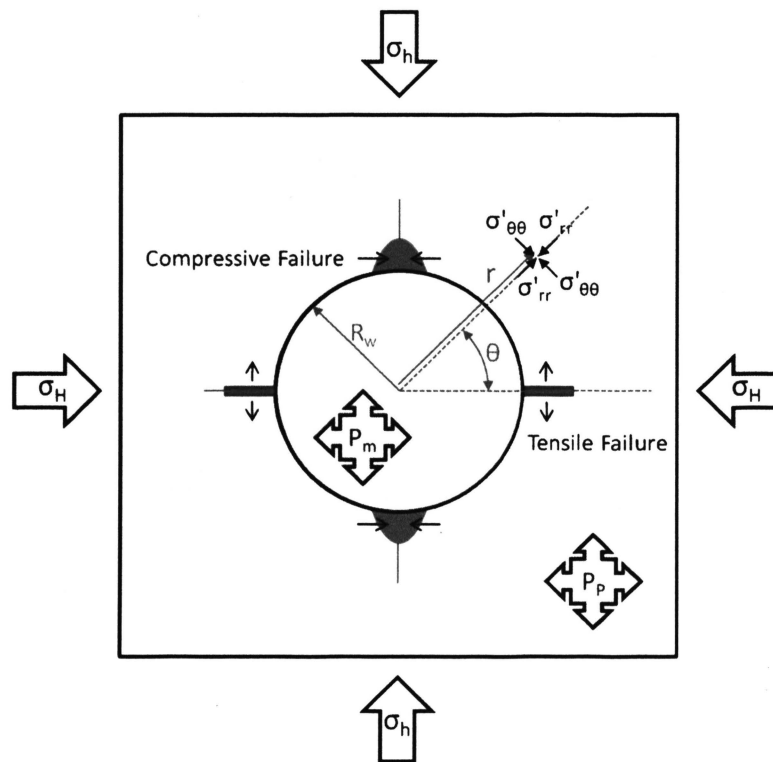


Figure 2.3. The effective stresses in cylindrical coordinate system and failure types around the borehole.

2.3. ROCK FAILURE CRITERIONS

2.3.1. Compressive Failure. Compressive failure in a wellbore, which is also termed breakout or collapse, occurs when the compressive strength of the formation is exceeded and the wellbore wall fails in shear. In order to predict rock failure and wellbore instability, different strength and failure criteria are commonly used. These criteria can be categorized into criteria where failure is dependent on the differential stress from the maximum and minimum principal stresses ($\sigma_1 - \sigma_3$) or into criteria which additionally account for the intermediate principal stress (σ_2). The most widely used

linear criteria are the Mohr-Coulomb failure criterion and the Drucker-Prager failure criterion [18]. The Mohr-Coulomb failure criterion assumes that only the differential stress is crucial for failure and that the intermediate principal stress has zero influence on rock strength/failure. The Drucker-Prager criterion puts the same weight on the intermediate principal stress as on the maximum and the minimum principal stresses [19]. It is known that the intermediate principal stress has a strengthening effect to the rock, but this strengthening effect is not as profound as predicted by the Drucker-Prager criterion [18]. Thus, the Drucker-Prager criterion tends to give over-optimistic rock strength, while the Mohr-Coulomb criterion tends to give conservative rock strength. Studies have shown that the choice of the applied failure criterion has a significant influence on the prediction of the safe minimum mud weight [20, 21, 22].

The numerical models of this study are linear elastic and isotropic, i.e. consistent with Kirsch's solution, and no failure will occur in the numerical model. Thus, the subsequent analysis on the rock failure is based on the numerical results from the elastic model without permanent deformation or failure. The Mohr-Coulomb failure criterion [23], as the most conservative criterion, is chosen for determining compressive failure and predicting the minimum mud weight for wellbore stability. Rock would fail when the shear stress, τ , developed on a specific plane reaches a value that overcomes the cohesion of the rock and the internal friction force between the opposing planes. The criterion is written as a linear function:

$$\tau = C_0 + \sigma_n \tan \phi \quad (19)$$

where τ is the shear stress, C_0 is the cohesion, ϕ is the internal friction angle of the rock, and σ_n is the normal stress on the failure plane. When the Mohr circle defined by σ_1 and σ_3 intersects with the failure envelope (Figure 2.2), shear failure will occur, and the relation of σ_1 and σ_3 at failure can be expressed in terms of C_0 and ϕ as below:

$$\sigma_1 = 2C_0 \frac{\cos \phi}{1 - \sin \phi} + \frac{1 + \sin \phi}{1 - \sin \phi} \sigma_3 \quad (20)$$

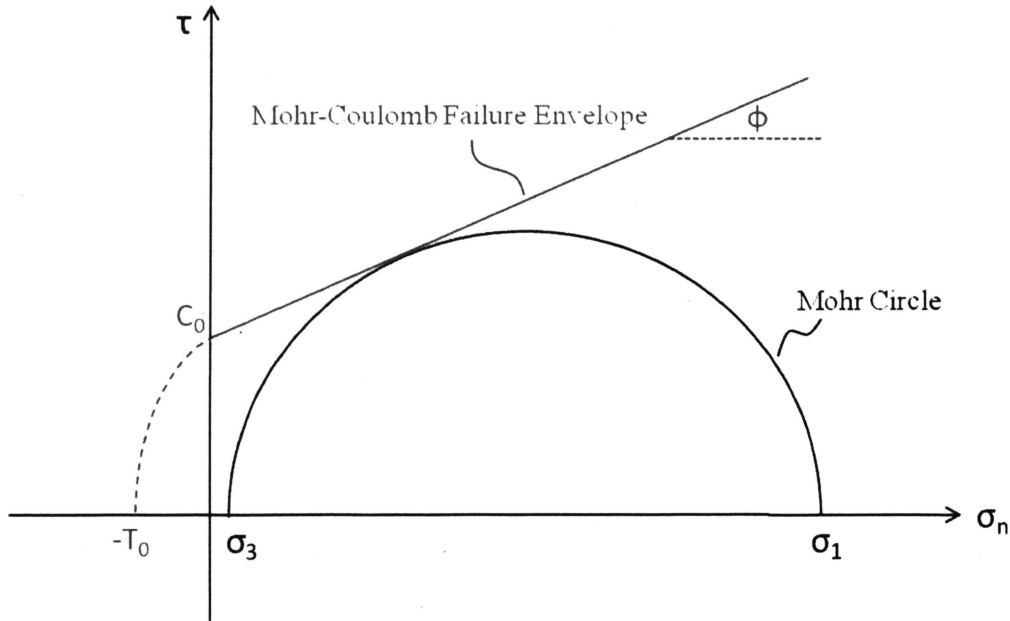


Figure 2.4. Mohr circle diagram showing compressive failure as the Mohr Circle touches the Mohr-Coulomb failure envelope.

2.3.2. Tensile Failure. Rocks hardly carry tensile stress and the tensile strength of rocks is as low as a few MPa [16]. Tensile fractures occur around wellbores when the hoop stress exceeds the tensile strength of the rock. This can be either a natural process or associated to the drilling process that forms the joints (i.e. drilling induced tensile failure) in rock. Hydraulic fracturing operations further increase the wellbore fluid pressure and deliberately fracture the formations an application of the tensile failure to increase formation permeability with the utilization of proppants to keep the fractures open. Tensile failure may cause drilling fluid loss and lost circulation in the wellbore. The criterion for tensile failure at the borehole wall is satisfied when the minimum principal stress σ_3 is equal or less than the formation tensile strength T_0 :

$$\sigma_3 \leq -T_0 \quad (21)$$

2.4. EFFECT OF PORE PRESSURE AND MUD PRESSURE TO FORMATION FAILURE

Pore pressure and mud pressure change the state of stress around the wellbore, acting as factors for wellbore stability. According to Equations (13) and (14), both pore pressure and mud pressure influence the hoop and radial stresses around the wellbore. Increasing pore pressure will offset the Mohr circle to the left in the Mohr circle diagram, leading to a higher chance of borehole breakout or tensile fracture depending on the magnitude of the differential stress (i.e. the size of the Mohr circle; Figure 2.5).

Increasing mud pressure will decrease the hoop stress and increase the radial stress, contributing to a smaller Mohr circle such that wellbore stability is improved. Nevertheless, if mud pressure is too high, it will cause tensile hoop stress and thus drilling-induced tensile fractures may occur (Figure 2.6).

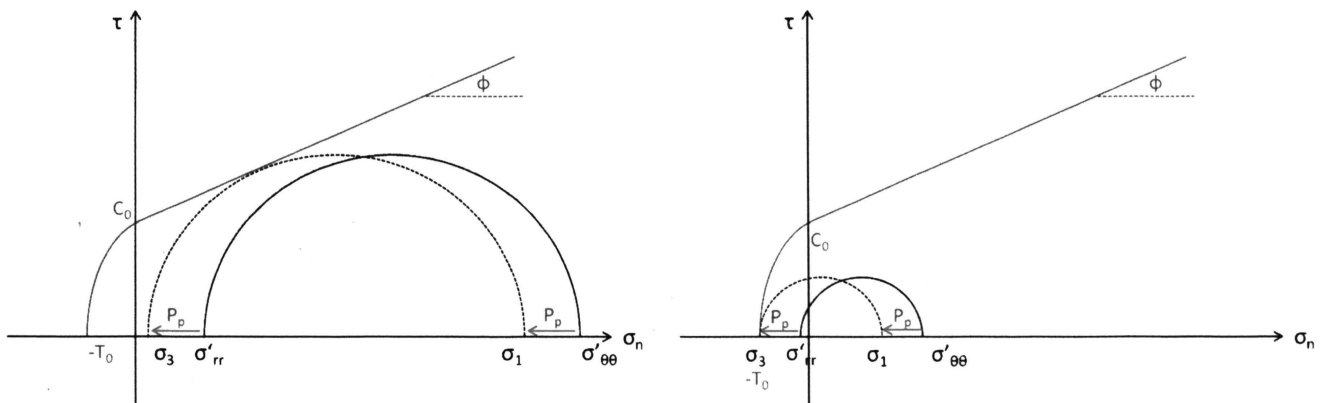


Figure 2.5. Influence of pore pressure toward formation failure.

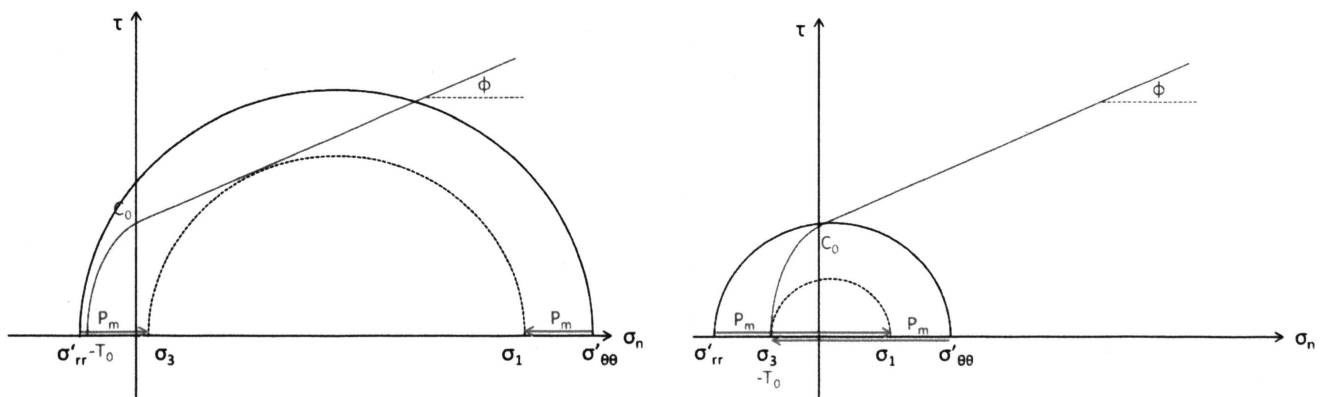


Figure 2.6. Influence of mud pressure toward formation failure.

2.5. SAFE MUD WEIGHT WINDOW

Drilling mud serves several functions in well drilling: it lubricates and cools the bit as it breaks up the rock at the bottom of the hole; it carries the rock cuttings to the surface where the cuttings are removed from the drilling fluid before it is re-circulated; it also helps control pressures in the wellbore to prevent from blowout; and it is a source of downhole information. For wellbore stability, mud pressure is required to be higher than the formation pressure to keep the formation fluid from entering the borehole, and should also be higher than the collapse pressure, which is the minimum mud pressure in the borehole to prevent the onset of shear failure. Thus, the lower limit of the safe mud weight window for drilling is defined by either the formation pressure and or the collapse pressure, i.e. the higher value determines the lower limit. The upper limit of the safe mud weight window is defined by the breakdown pressure, the maximum mud pressure to avoid the onset of tensile failure.

Based on the Mohr-Coulomb failure criterion, the collapse pressure can be obtained at 90 degrees at the borehole wall by utilizing the σ_1 - σ_3 relation in Equation (20) and the fact that the center of the Mohr circles (i.e. the mean stress) stays the same (Equation (22)) when the mud pressure changes:

$$\frac{\sigma'_{rr} + \sigma'_{\theta\theta}}{2} = \frac{\sigma_3 + \sigma_1}{2} \quad (22)$$

$$\Rightarrow \sigma_3 = \frac{\sigma'_{rr} + \sigma'_{\theta\theta} - 2C_0 \frac{\cos \phi}{1 - \sin \phi}}{1 + \frac{1 + \sin \phi}{1 - \sin \phi}} \quad (23)$$

Thus, the collapse pressure can be obtained as:

$$\begin{aligned} P_{m,collapse} &= \sigma_3 - \sigma'_{rr,90deg} \\ &= \frac{\sigma'_{rr,90deg} + \sigma'_{\theta\theta,90deg} - 2C_0 \frac{\cos \phi}{1 - \sin \phi}}{1 + \frac{1 + \sin \phi}{1 - \sin \phi}} - \sigma'_{rr,90deg} \end{aligned} \quad (24)$$

The breakdown pressure is the maximum mud pressure to prevent onset of tensile failure for which the hoop stress at 0 degrees equals the tensile stress of the rock:

$$\begin{aligned}\sigma'_{\theta\theta,0\text{ deg}} - P_{m,\text{breakdown}} &= -T_0 \\ \Rightarrow P_{m,\text{breakdown}} &= \sigma'_{\theta\theta,0\text{ deg}} + T_0\end{aligned}\quad (25)$$

2.6. FINITE ELEMENT ANALYSIS

2.6.1. Governing Equation in Finite Element Modeling. In continuum mechanics, an object is treated as a continuous mass, instead of as discrete particles for its kinematics and mechanic behavior. Based on the fundamental physical laws applying on the continuum object partial differential equations describing deformation of a continuous rock formation can be derived. From the law of conservation of momentum, the continuum form of this principle can be derived as follows [8, 24, 25]:

$$\frac{\partial \sigma_{ij}}{\partial x_j} + \rho b_i = \rho \frac{dv_i}{dt} \quad (26)$$

where ρ is the density of the material, and b_i is the body force, and v_i is the velocity of the object. Neglecting the acceleration term (as considered appropriate for rock deformation), Equation (18) can be expressed as

$$\frac{\partial \sigma_{ij}}{\partial x_j} + \rho b_i = 0 \quad (27)$$

This equation can also be derived from the law of equilibrium of forces acting on an infinitesimal element of dimension dx, dy, dz . The force equilibrium of the infinitesimal element in x-direction is:

$$\begin{aligned}
& \left(\sigma_{xx} + \frac{\partial \sigma_{xx}}{\partial x} dx \right) dydz - \sigma_{xx} dydz + \left(\sigma_{yx} + \frac{\partial \sigma_{yx}}{\partial x} dx \right) dx dz - \sigma_{yx} dx dz \\
& + \left(\sigma_{zx} + \frac{\partial \sigma_{zx}}{\partial x} dx \right) dydz - \sigma_{zx} dydz + \rho b_i = 0
\end{aligned} \tag{28}$$

Similar equations can be derived for the y- and z-directions, and the same equation as Equation (27) can be obtained.

Hook's law provides a stress-strain relationship for linear elasticity, and the strain tensor is presented in terms of displacement:

$$\sigma_{ij} = c_{ijkl} \varepsilon_{kl} \tag{29}$$

$$\varepsilon_{ij} = \frac{1}{2} \left(\frac{\partial u_i}{\partial x_j} + \frac{\partial u_j}{\partial x_i} \right) \tag{30}$$

Where c_{ijkl} is the stiffness matrix of the material, ε_{kl} is the strain tensor, and u_i is the displacement. Thus, Equation (27) can be re-written as the governing partial differential equation for the stress-displacement problem:

$$\frac{\partial}{\partial x_j} \left[c_{ijkl} \frac{1}{2} \left(\frac{\partial u_i}{\partial x_j} + \frac{\partial u_j}{\partial x_i} \right) \right] + \rho b_i = 0 \tag{31}$$

With appropriate boundary conditions, solutions may be obtained from the above PDE for the continuum object.

2.6.2. Finite Element Method. However, partial differential equations may not always have solutions when the physical problem is complex in geometry, material properties, boundary conditions, etc. The finite element method provides a numerical method to solve for approximate solutions of partial differential equations. In the finite element method, the continuum of the object is broken into discrete elements, and the

continuity of the solution is maintained at nodal points where the elements are connected to each other. Each element is governed by a linear equation derived from the governing PDE with the utilization of an approximation of the solution u :

$$K^e u^e + f^e = q^e \quad (32)$$

where K^e is the element stiffness matrix, f^e is the element loading, and q^e is the internal force at the element nodes.

The solution u in the original PDE is approximated with \hat{u} in each element, by means of shape functions N_i that account for the solutions between nodal solutions u_i :

$$u \approx \hat{u} = \sum_i N_i u_i \quad (33)$$

Assembling the equations for all the elements in the discrete system, a global matrix form of the equations of the physical problem can be obtained, and numerical results, i.e. the displacement in the physical problem in this study, can be found accordingly. Strain and stress can be subsequently derived from the displacement.

2.6.3. Error Source and Approximation. Figure 2.7 shows the steps of a simulation process for physical problems [25]. Physical systems are often complicated with numerous parameters to deal with, and thus are idealized into mathematical equations including assumptions and simplifications describing the physical problem. The mathematical model has to be adjusted and calibrated with experimental measurements to present the physical system correct enough in a mathematical way. Errors may occur in this idealization process since the physical problem is simplified with assumptions. Another error results from discretizing the continuum itself. The solution of the numerical model is sensitive to both the spatial resolution of the FE mesh and to the order of the approximation functions (i.e. shape functions).

The comparison of the numerical solution and the analytical solution is demonstrated in Figure 2.8. Utilizing a fine discretization (shown in red lines), the numerical solution provides a better fit to the analytical solution than the solution of the coarse discretization (shown in blue lines). In addition to the discretization, a linear approximation (later referred to as 1st order elements) between nodal solutions is another important reason that the accuracy of the numerical solution is limited. Quadratic approximations (later referred to as 2nd order elements) can effectively minimize the errors generated by the continuum discretization.

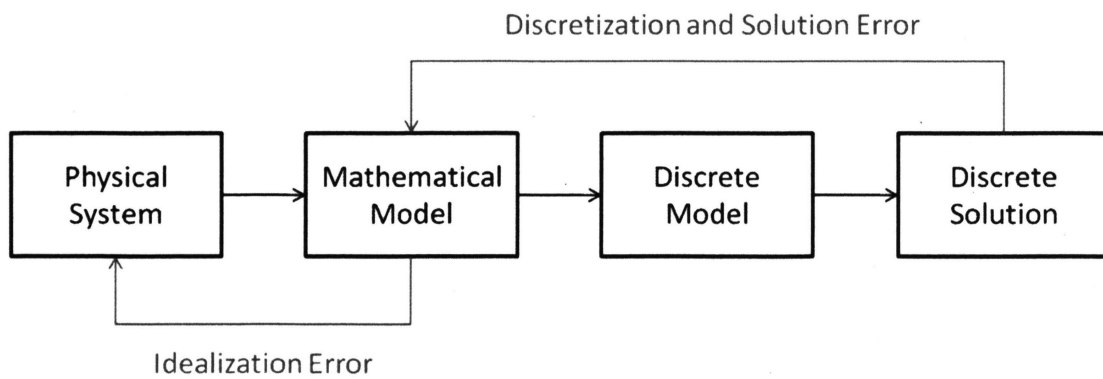


Figure 2.7. Process for FE simulation of physical problem.

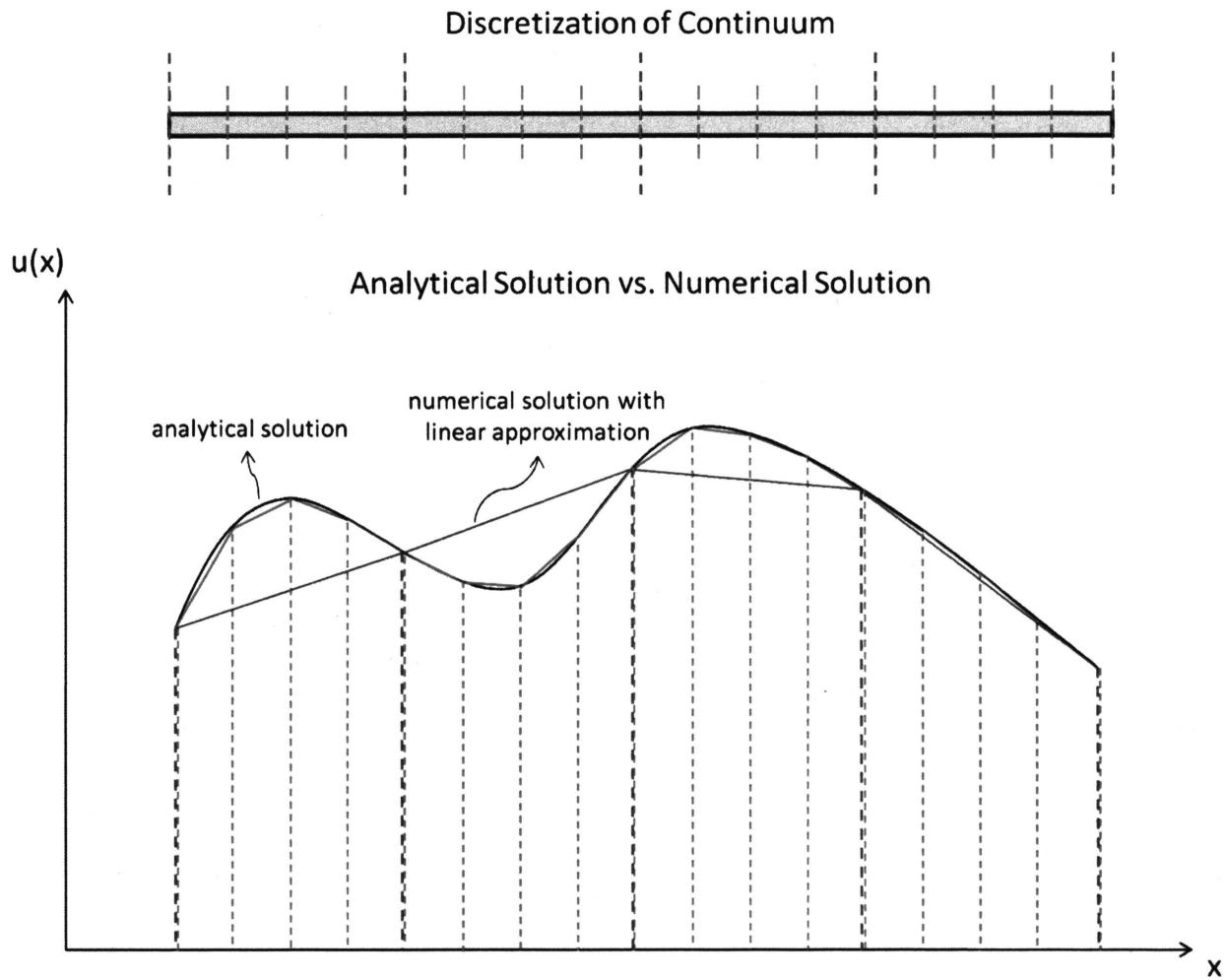


Figure 2.8. A schematic view showing the analytical solution of the continuum and the numerical solution of the two discrete systems. The continuum is discretized by either blue lines or red lines. When a continuum is discretized into more sub-regions (shown in red), errors from the numerical can be decreased. The use of linear approximation is also a source of the errors, and the approximation can be improved by using quadratic shape function.

3. GEOMECHANICAL MODEL AND MODELING APPROACH

3.1. MODEL SETTINGS

An initial 2-D base model of a vertical borehole is setup as a reference for the sensitivity check of the various meshing parameters. A compilation of various models with changing model sizes, refinement of the discretization and different boundary conditions (i.e displacement, stress, and drilling simulation boundary conditions) are also generated. Parametric studies are conducted for these models and compared with the base model and the analytic solution. Finally an optimization procedure of modeling and meshing parameters to minimize the numerical error is developed.

The 2-D base model has a borehole radius of 0.1m (R_w) and horizontal dimensions of 2m by 2m (Figure 3.1). For a clearer understanding the model is divided into several regions. The near-wellbore region ranges from the borehole wall (R_w) to the outer circle of the region ($5R_w$); the far-field region ranges from the outer circle of the near-wellbore region ($5R_w$) to the model boundary ($10R_w$). The base model mesh consists of 1st order quadrilateral 2-D plane strain pore pressure elements. Referring to Figure 3.1, for the circumferential mesh density in the near-wellbore region, 20 elements per quarter circumference are used; for the initial radial mesh density, 20 elements per $4R_w$ distance are used; for the far-field region a radial mesh density of 10 elements per $5R_w$ distance is used. These element densities are representative of commonly regarded good quality meshes [26], i.e. we have a fine mesh in areas of rapidly changing stresses and the element aspect ratio (optimal is 1) does not exceed 2.55 in the near wellbore region.

The geometry and mesh of the 3-D wellbore models are built from the 2-D base and optimized 2-D models. An additional sensitivity check is conducted for the model and element height as well as the element type. The 3-D model results are compared with the 2-D models and the analytical solutions. For the sensitivity analysis, the 3-D base model features the exact same discretization as the 2-D base model for the borehole opening plane (i.e. horizontal plane). The model height is 10m and with an element height of 1m (Figure 3.2). The element type used here is 1st order quadrilateral 3-D pore pressure element.

The numerical models are solved with the commercial Finite Element software package ABAQUS™.

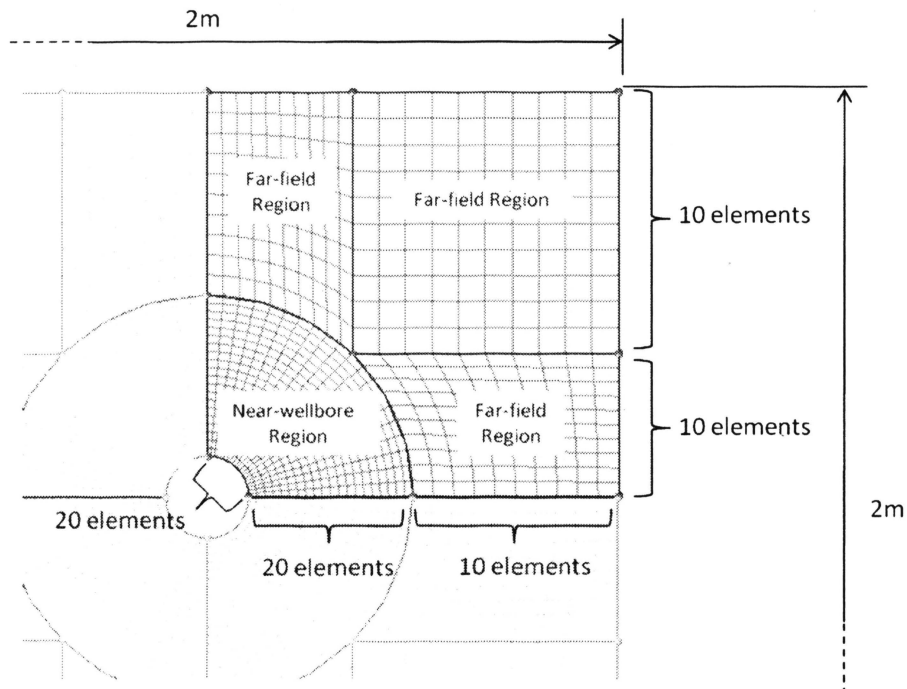


Figure 3.1. The 2-D base model using a mapped meshing approach and varied mesh densities in the sub-regions.

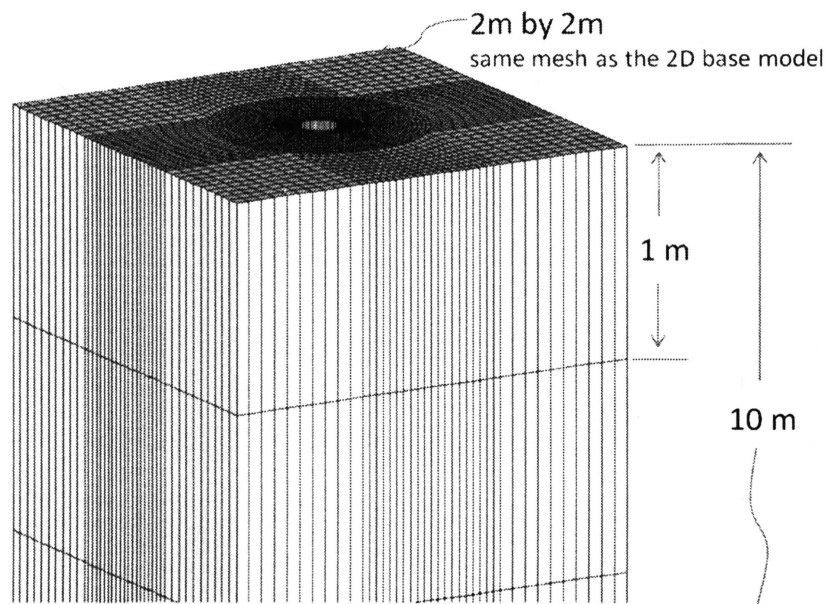


Figure 3.2. The 3-D base model generated from the 2-D cross-section.

3.2. MAPPED MESHING APPROACH

The geometry of a borehole model has been constructed using the commercial pre-processing software package Altair HyperMesh™. For the 2-D wellbore model, a mapped meshing approach [27] was followed to have complete control on the size and shape of the elements. By using this meshing approach, the overall wellbore geometry is organized into several sub-regions such that the mesh generated by an automated meshing algorithm in HyperMesh yields a minimal number of odd-shaped elements, and the mesh size and aspect ratio of the elements around the borehole can be controlled most conveniently. Referring to Figure 3.1, in the near-wellbore region, relatively fine circular meshes are used around the borehole, since the state of stress changes rapidly close to the borehole wall. In the outer far-field regions, coarser meshes are used since the state of stress in this region is given by the homogeneous far-field stresses. The near-wellbore region is defined as four times of borehole radius (R_w), ranging from R_w to $5R_w$ from the borehole center.

For the construction of the 3-D wellbore model, the model is built initially in 2-D as the wellbore cross-section following the mapped meshing approach, and then dragged along the wellbore axis to complete the 3-D model and mesh.

3.3. MODEL INPUT AND BOUNDARY CONDITIONS

The material behavior of the model is linear elastic, isotropic and homogeneous throughout the overall geometry. The material uses common sandstone material parameters of a Poisson's ratio of 0.25 and a Young's modulus of 15 MPa. The initial anisotropic far-field stresses are: $\sigma_H = 40$ MPa and $\sigma_h = 20$ MPa; the fluid pressures are: $P_p = 10$ MPa and $P_m = 15$ MPa. For the 2-D model plane strain analysis is utilized.

The influence of the various meshing parameters on the quality of the results is studied by using three types of boundary conditions:

(1) displacement boundary conditions: far-field stresses are generated by applying displacements to the model boundary (Figure 3.3 (a));

(2) stress boundary conditions: far-field stresses are directly applied on the model boundaries (Figure 3.3 (b));

(3) drilling process simulation: the model initially represents an undisturbed formation of rock (i.e. borehole is not existent) and is pre-stressed to simulate the initial state of stress in equilibrium in the formation before drilling; with the removal of wellbore elements, the drilling process is simulated and subsequently the stresses are redistributed (Figure 3.3 (c)).

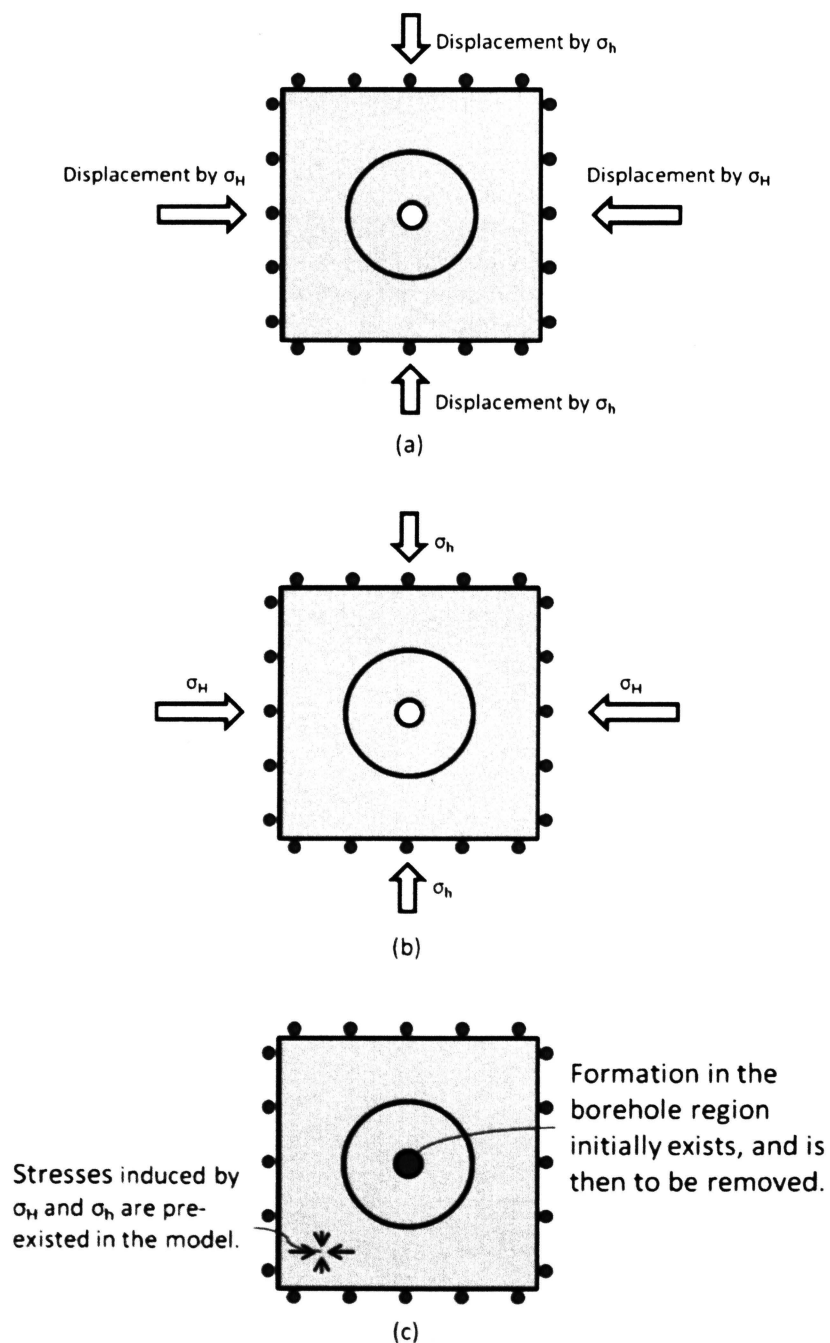


Figure 3.3. Three types of boundary conditions: (a) displacement; (b) stress; (c) drilling process simulation.

3.4. PARAMETRIC STUDY

For the 2-D wellbore model, sensitivity analyses are conducted for the following parameters of the model/mesh: (1) model size; (2) element type; (3) mesh density in the near-wellbore region and far field region.

For each parameter the modeled result is compared to the analytical solution, and the influence of the model parameters is studied.

The model size is adjusted in terms of multiplying factors of the borehole diameter. The model size is a crucial factor because if the model is too small with respect to the borehole size, the modeled results will not yield homogenous far-field stresses around the model boundary and thus the results are also influenced in the near-wellbore region.

Different element types, i.e. quadrilateral 1st and 2nd order and triangular 2nd order elements, are studied. It should be mentioned that triangular 1st order elements are not considered in this study because they do not handle pore pressure. In the finite element method, different element types have their unique shape function and thus will lead to varied numerical solutions.

Utilizing a mapped meshing approach, the mesh density can be varied separately for the near-wellbore region and the far-field region. This is convenient because the state of stress changes rapidly in the near-wellbore region and is more uniform in the far-field. The finer meshes in the near-wellbore region can accommodate for the dramatic changes more precisely, while less elements in the far-field can sufficiently accommodate or the minor changes without wasting computing resources or time. For the sensitivity analysis the mesh density around the circumference of the borehole in the near-wellbore region and the mesh density along the radial distance in the near-wellbore and in the far-field region are investigated.

For 3-D wellbore model, the height of model size and element size is further investigated. The influence of these parameters is compared to the 2-D modeled results and the analytical solution. Element types used in the parametric study are quadrilateral 1st and 2nd order elements, in full and reduced integration point of the element where stress results are obtained in the finite element analysis.

4. RESULTS

4.1. 2-D WELLBORE MODEL USING DISPLACEMENT BOUNDARY CONDITIONS

4.1.1. Comparison of the Base Model Results to the Analytical Solution.

Figure 4.1 gives a general impression of the stress anisotropy (here for the S11 component) around a wellbore for the base case model. The far-field stress at 0° near the boundary is homogeneous (34.2 MPa, corresponding to σ_H 40 MPa) and near the wellbore the magnitude changes from 6.8 MPa to 15.2 MPa. In order to assess the quality of the numerical results the hoop and radial stresses at 0° and 90° is compared with the analytical solution (Figure 4.2). The hoop stress at 0° with respect to σ_H or the radial stress at 90° matches the analytical solution throughout the model. However, the hoop stress at 90° and the radial stress at 0° show discrepancies. These misfits are especially noticeable at the borehole wall for the hoop and radial stresses at either 0° or 90° . Table 4.1 shows the errors of the effective stresses at borehole wall of the base model. The errors have maximum values of -8.23 MPa at the borehole wall for the hoop stress at 90° , and 4.62 MPa for the hoop stress at 0° .

The significance of these numerical errors becomes obvious when considering that the hoop stress at 90° is related to compressive failure of the wellbore, while the hoop stress at 0° is related to tensile failure of the wellbore. This shows the inherent need to develop a mesh optimization procedure that provides precise results for wellbore models.

Table 4.1. Errors of the effective stresses at borehole wall for the 2-D base model.

Numerical Errors at Borehole Wall (MPa)			
$\sigma_{\theta\theta}$ at 0°	σ_{rr} at 0°	$\sigma_{\theta\theta}$ at 90°	σ_{rr} at 90°
4.62	2.58	-8.23	0.10

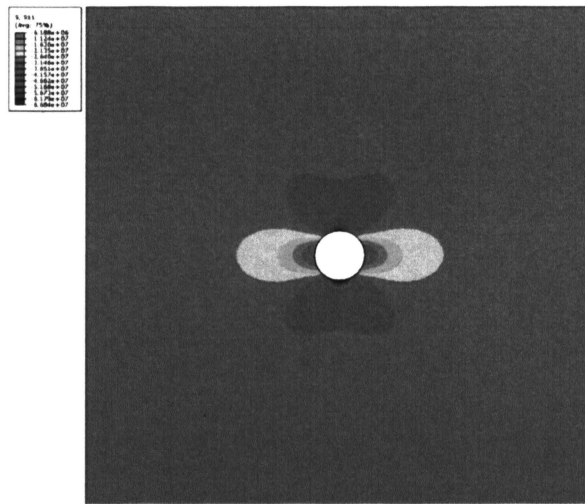


Figure 4.1. S11 distribution in the 2-D wellbore model.

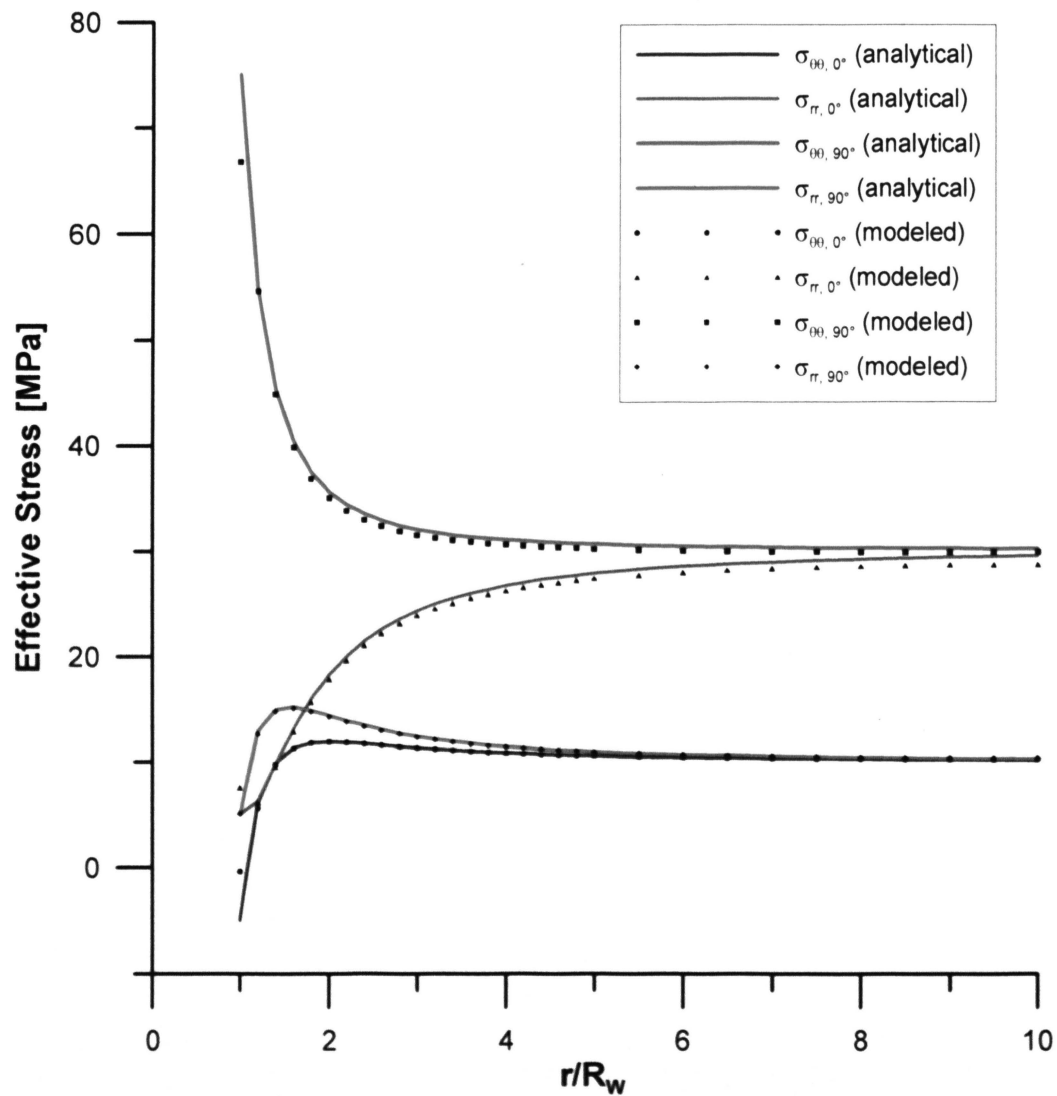


Figure 4.2. The modeled results from the base model as compared to the analytical solution.

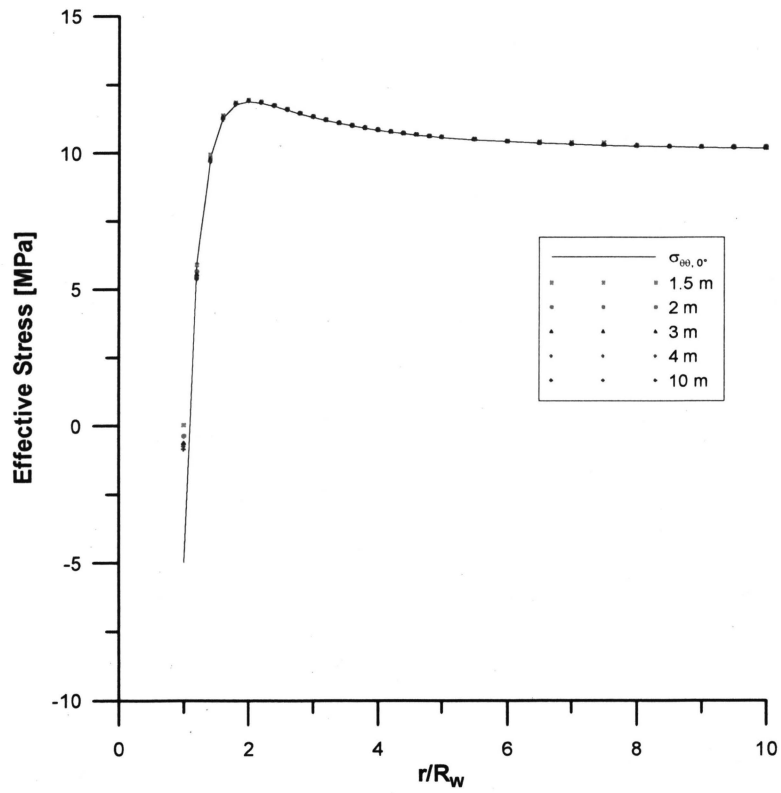
4.1.2. Sensitivity Analysis of Model Size. For the sensitivity analysis of the model size, in addition to the base model (2m by 2m; i.e. 10x of borehole diameter), models of 1.5m by 1.5m (7.5x of diameter), 3m by 3m (15x of diameter), 4m by 4m (20x of diameter), 10m by 10m (50x of diameter) are investigated.

Choosing the overall model size is the first step when modeling a geometric structure. If the model size is chosen appropriately, the state of stress at the boundary of the model should reach the homogeneous far-field stresses σ_H and σ_h . The sensitivity analysis of the model size shows that the finite element results are affected by the model size, not only as expected for the far-field region but also in the near-wellbore region (Figure 4.3). This can be seen most clearly for the radial stress at 0° (Figure 4.3(b)).

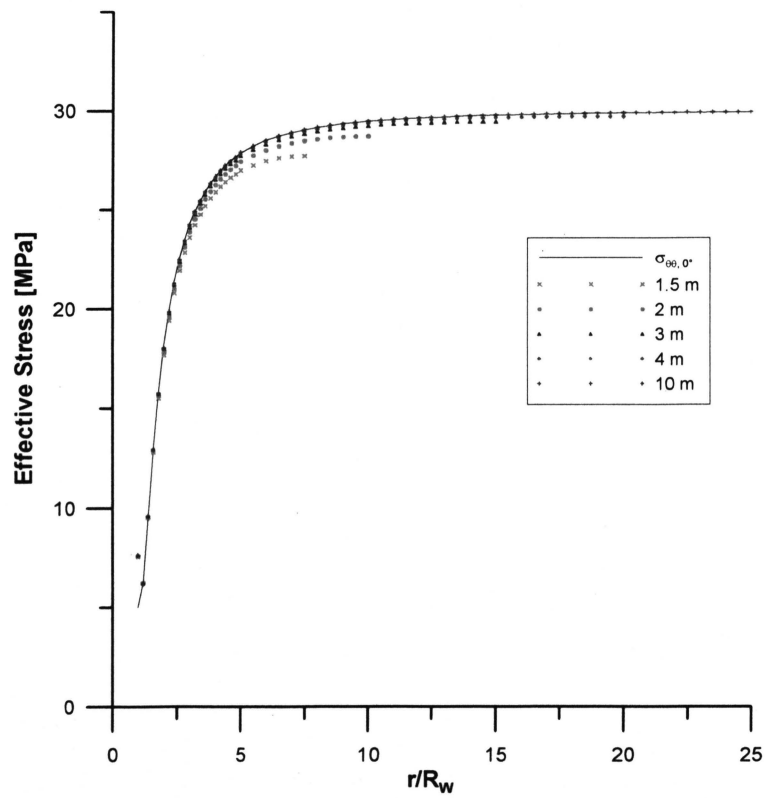
Larger model size provides an overall better fit of the model results to the analytical solution. Further, increasing the model size specifically improves the model results for the hoop stress at the borehole wall at 90° (Table 4.2), which shows the largest error in the base model. However, the errors at the borehole wall do not decrease to a satisfactory degree. From the 1.75m model to the 10m model, the hoop stress at borehole wall at 90° is improved by 2.34 MPa, but the error in the 10m model is still as high as -6.91 MPa.

The 3m and 4m models, which are 15 and 20 times of the borehole diameter (0.2 m), respectively, produce a result in good agreement with the analytical solutions for the effective stresses, and larger model dimension as 50 times of the borehole diameter only improves the fitting marginally.

When the model dimension is not large enough, the modeled far-field stresses have a great discrepancy to the actual far-field stresses acting on the model, and simultaneously the modeled stresses in the near-wellbore region is adversely affected in matching the analytical solution. It should be noted that wellbore failure may occur on the wellbore surface and inside the formation [28], thus the importance of the fitting in the near-wellbore region, in addition to at the borehole wall, should not be ignored.

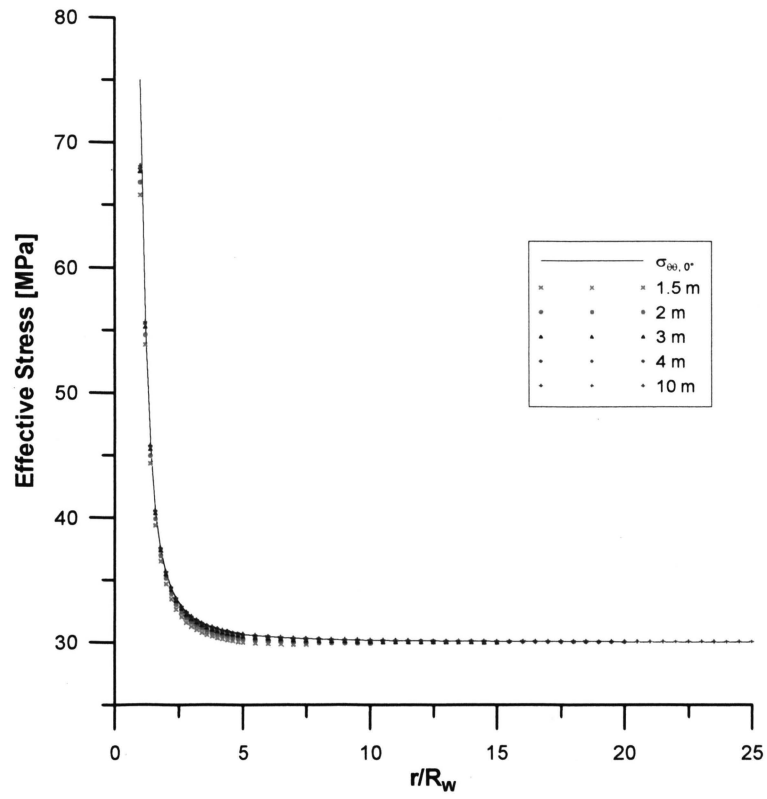


(a)

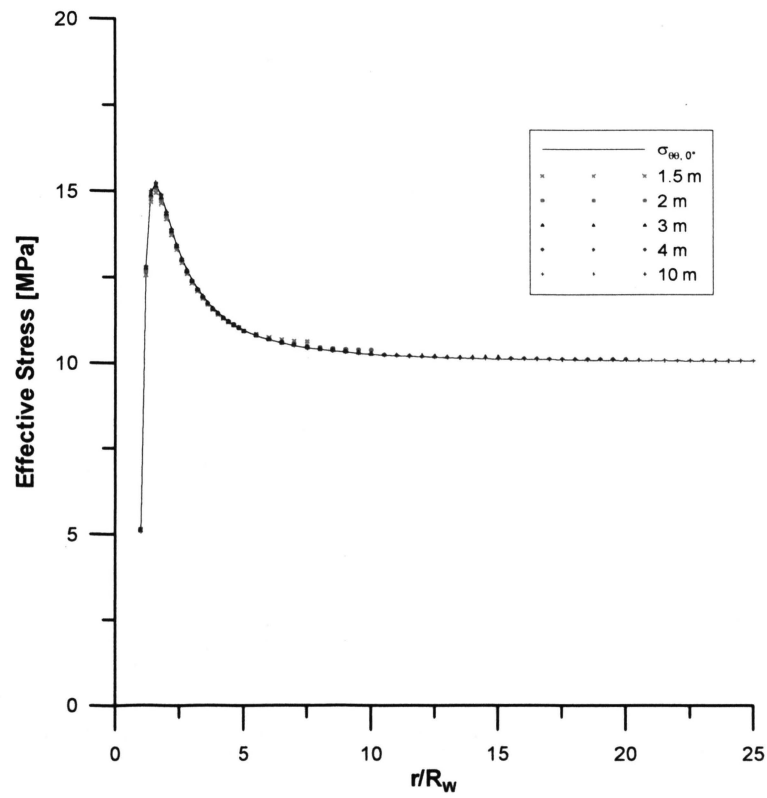


(b)

Figure 4.3. Influence of model size on the effective stresses at: (a) $\sigma_{\theta\theta}$ at 0° and (b) σ_{rr} at 0° .



(c)



(d)

Figure 4.3. (Continued) Influence of model size on the effective stresses at: (c) $\sigma_{\theta\theta}$ at 90° and (d) σ_{rr} at 90° .

Table 4.2. Sensitivity analysis of the model size using displacement boundary conditions.

Model Size (m)	Numerical Errors at Borehole Wall (MPa)			
	$\sigma_{\theta\theta}$ at 0°	σ_{rr} at 0°	$\sigma_{\theta\theta}$ at 90°	σ_{rr} at 90°
1.75	5.02	2.55	-9.25	0.11
2	4.62	2.58	-8.23	0.10
3	4.38	2.64	-7.37	0.09
4	4.25	2.62	-7.14	0.10
10	4.14	2.63	-6.91	0.09

4.1.3. Sensitivity Analysis of Element Type. For the sensitivity analysis of the element type, 1st (base model) and 2nd order quadrilateral and 2nd order triangular pore pressure elements, which are referred to as CPE4P, CPE8P, and CPE6P in ABAQUSTM, are studied. 1st order triangular elements are not used here because pore pressure cannot be applied for this element in ABAQUSTM.

The results show that all three types of elements yield very similar results beyond $r/R_w = 2$ (Figure 4.4). However, at the borehole wall, quadrilateral 2nd order elements and triangular 2nd order elements greatly improve the results compared to quadrilateral 1st order elements, and the maximum error at the borehole wall can be greatly reduced to around -1.25 (quads) or -0.13 (trias) MPa from -8.23 MPa of the base model (Table 4.3). Although the 2nd order triangular element produces slightly better results than the quadrilateral 2nd order element at the borehole wall, the results from quadrilateral 2nd order elements generally have less discrepancies compared to the analytical solution in the region of $r/R_w = 1$ to 2. Thus the quadrilateral 2nd order element should be chosen over the triangular 2nd order element to obtain an overall better fitting to the analytical solution.

Table 4.3. Sensitivity analysis of the model size using displacement boundary conditions.

Element Type	Numerical Errors at Borehole Wall (MPa)			
	$\sigma_{\theta\theta}$ at 0°	σ_{rr} at 0°	$\sigma_{\theta\theta}$ at 90°	σ_{rr} at 90°
1st Quad	4.62	2.58	-8.23	0.10
2nd Quad	0.50	-0.80	-1.25	0.50
2nd Tria	1.11	-0.63	-0.13	0.06

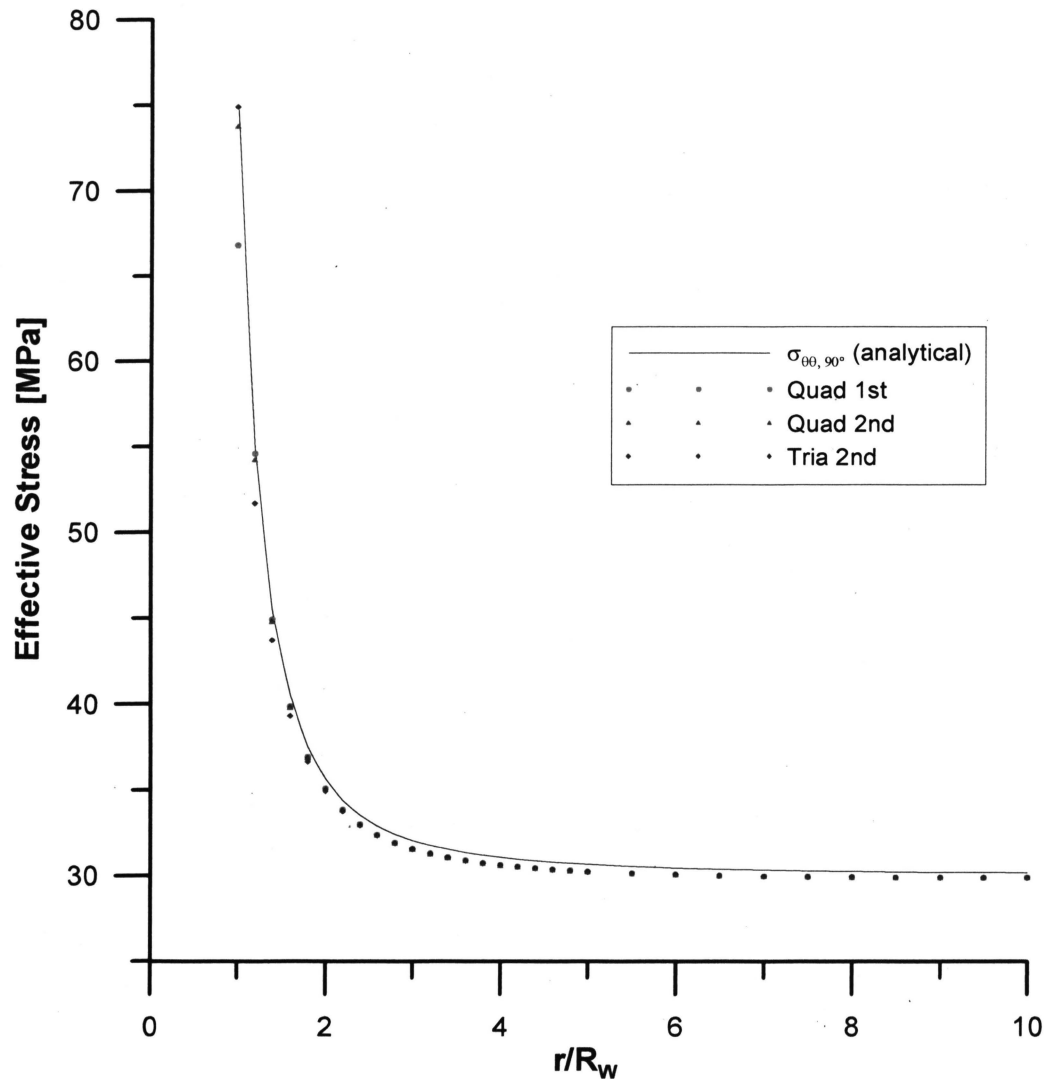


Figure 4.4. Influence of element type for the hoop stress at 90° .

4.1.4. Sensitivity Analysis of Mesh Density. For the sensitivity analysis of the mesh density in the near-wellbore region, the base model has a mesh density of 20 elements per quarter wellbore circumference and a mesh density of 20 elements per the radial distance. Mesh densities of 10, 30 and 40 elements per quarter wellbore circumference, mesh densities of 10, 30, 40, 50 elements per the $4R_w$ radial distance are studied.

A change in the circumferential mesh density has almost no effects to the model results near the borehole or for the overall fitting of the results in the entire model (Table 4.4). An increase in mesh density would adversely cause a slightly larger error, resulting

from a poorer aspect ratio of the elements due to the elongated shape, if the radial mesh density is remained fixed.

A change in the radial mesh density significantly alters the model results and by utilizing higher densities significant improvement can be obtained (Figure 4.5). This becomes most apparent for the hoop stress at 90° where the difference between the model results and the analytical solution decreases from -12.89 MPa for 10 elements to -4.72 MPa for 50 elements (Table 4.5). Also the difference for the radial stress at 0° decreases from 4.94 MPa for 10 elements to 1.08 MPa for 50 elements (Table 4.5). The influence of increasing the radial mesh density marginally decreases, and the accuracy of the effective stresses can be only enhanced to some degree by refining the mesh.

For the sensitivity analysis of the mesh density in the far-field region, the sensitivity analysis of 20 (base), 30, and 40 elements per the $5R_w$ -to- $10R_w$ distance from the borehole center shows no distinct differences in the modeled results. The mesh quality in the far-field is of no major concern to the results.

Table 4.4. Sensitivity analysis of the mesh density around the borehole circumference using displacement boundary conditions.

Circum. Density (elements)	Numerical Errors at Borehole Wall (MPa)			
	$\sigma_{\theta\theta}$ at 0°	σ_{rr} at 0°	$\sigma_{\theta\theta}$ at 90°	σ_{rr} at 90°
10	4.80	2.79	-8.39	0.05
20	4.62	2.58	-8.23	0.10
30	4.65	2.56	-8.22	0.13
40	4.65	2.55	-8.22	0.14

Table 4.5. Sensitivity analysis of the mesh density along the radial distance in the near-wellbore region using displacement boundary conditions.

Radial Density (elements)	Numerical Errors at Borehole Wall (MPa)			
	$\sigma_{\theta\theta}$ at 0°	σ_{rr} at 0°	$\sigma_{\theta\theta}$ at 90°	σ_{rr} at 90°
10	7.12	4.94	-12.89	-0.02
20	4.62	2.58	-8.23	0.10
30	3.58	1.76	-6.31	0.11
40	2.95	1.34	-5.28	0.08
50	2.93	1.08	-4.72	0.07

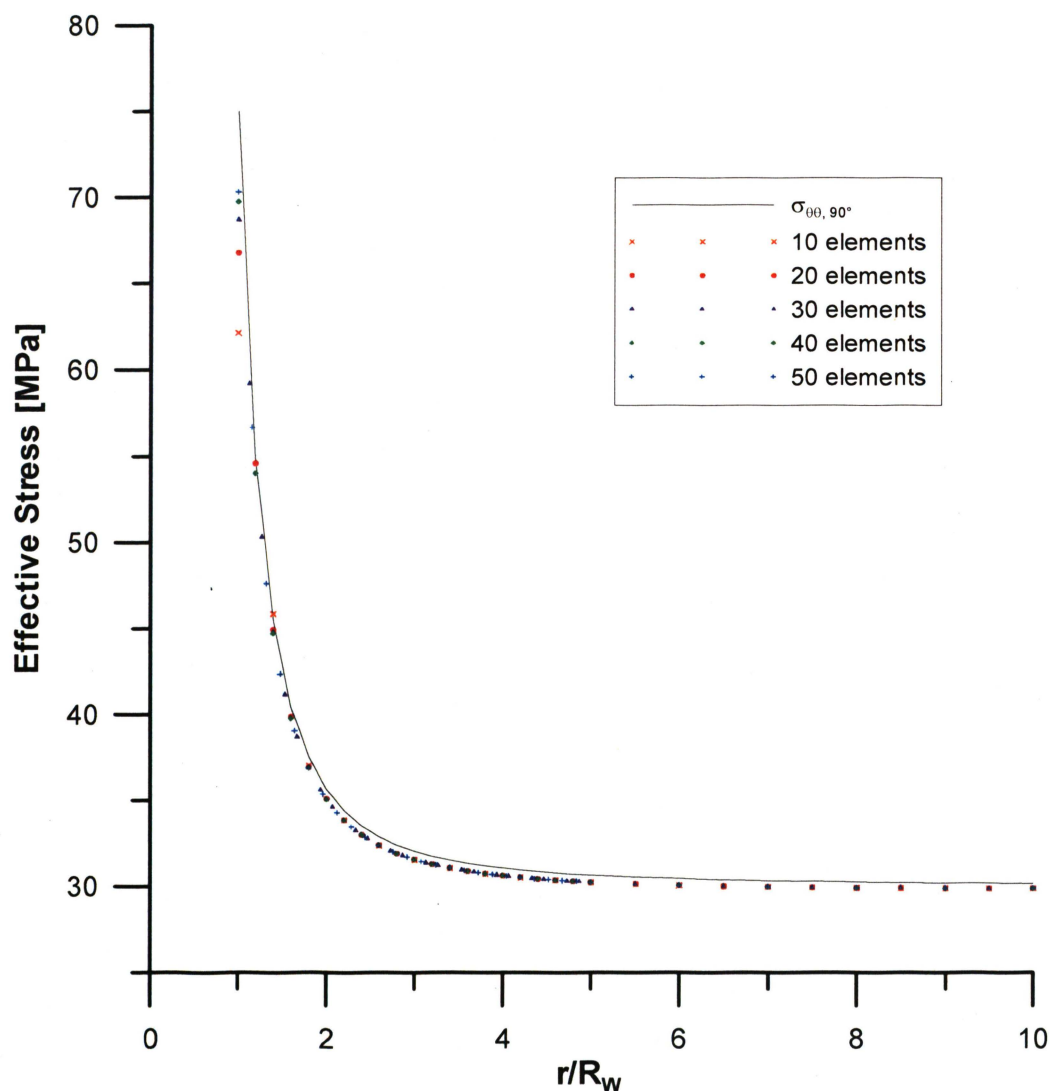


Figure 4.5. Influence of the radial mesh density in the near-wellbore region for the hoop stress at 90° .

4.1.5. General Meshing Guideline. From the sensitivity study presented for the displacement boundary conditions, a general guideline for meshing and the choice of meshing parameters can be obtained. To achieve good quality numerical results of borehole models, a general guideline of meshes can be summarized as follows:

- (1) use an appropriate model size to yield a good match to the analytical solution throughout the model;
- (2) use 2nd order quadrilateral elements to increase the accuracy of effective stresses at the borehole wall;
- (3) use a finer mesh along the radial distance in the near-wellbore region to further improve the results;

- (4) select appropriate mesh density along the borehole circumference corresponding to the mesh density in the radial distance in the near-wellbore region to ensure a good aspect ratio of the elements;
- (5) select appropriate mesh density in the far-field region corresponding to the mesh density in the near-wellbore region to keep good aspect ratio of the elements.

4.2. OPTIMIZATION OF 2-D WELLBORE MODEL

According to the parametric study and the guideline obtained above, an optimized model is constructed using the following parameters:

- Model size: 4m by 4m, which is 20x the borehole diameter.
- 2nd order quadrilateral element.
- Radial mesh density in the near-wellbore region: 40 elements along the $4R_w$ distance.
- Circumferential density in the near-wellbore region: 40 elements per quarter wellbore circumference.
- Radial mesh density in the far-field region: 40 elements along the $5R_w$ distance.

Comparing the numerical results from the optimized model to the analytical solution shows a very good agreement (Figure 4.6). The errors at the borehole wall are minimized to less than 0.5 MPa (Table 4.6).

Table 4.6. Errors of the modeled results from the optimized 2-D model compared to the base model.

Model	Numerical Errors at Borehole Wall (MPa)			
	$\sigma_{\theta\theta}$ at 0°	σ_{rr} at 0°	$\sigma_{\theta\theta}$ at 90°	σ_{rr} at 90°
Base	4.62	2.58	-8.23	0.10
Optimized	0.09	-0.29	-0.28	0.50

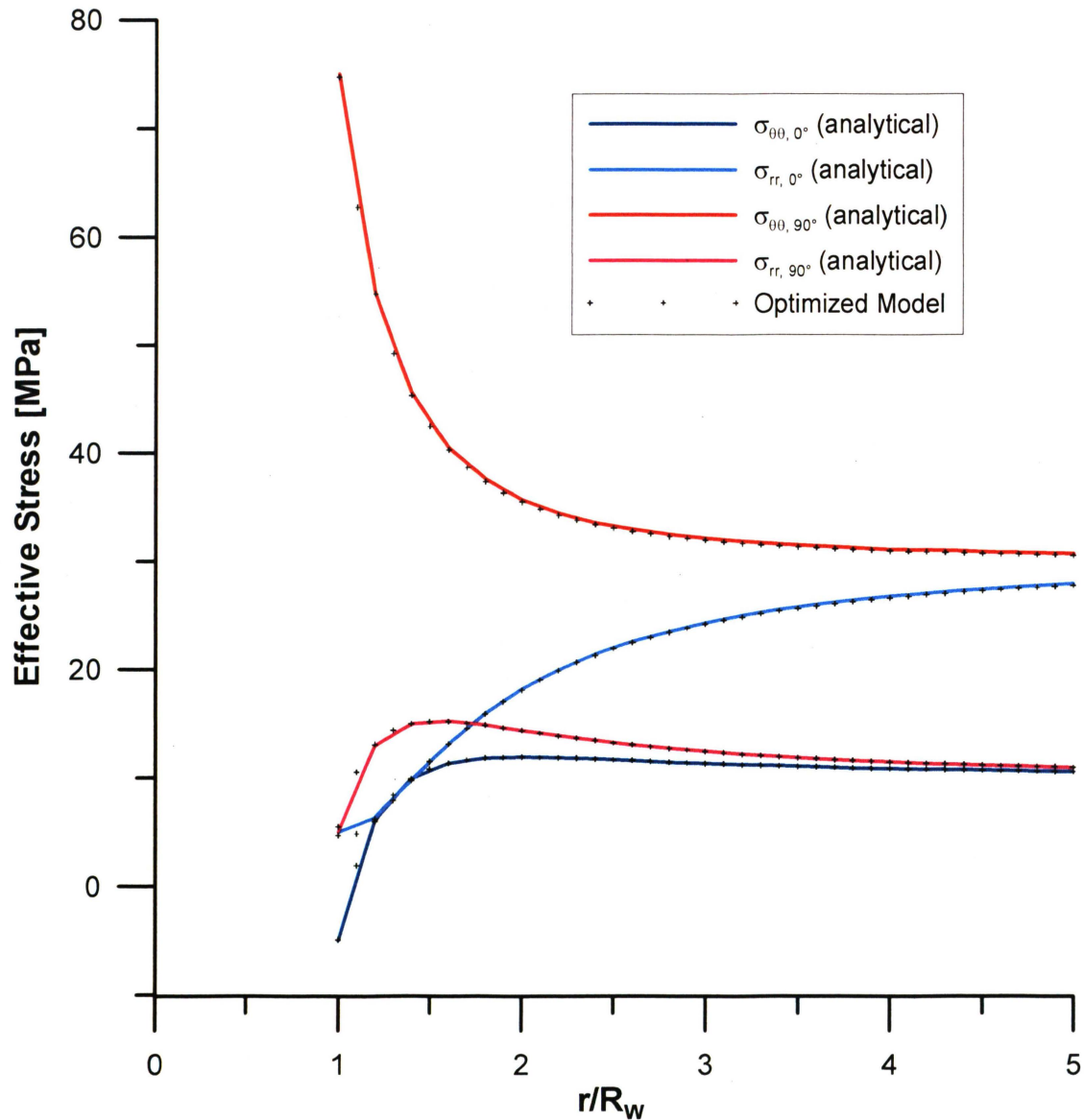


Figure 4.6. The modeled results from the optimized 2-D model compared to the analytical solutions.

4.3. 2-D WELLBORE MODEL USING STRESS BOUNDARY CONDITIONS AND DRILLING SIMULATION BOUNDARY CONDITIONS

The models using stress boundary conditions and drilling process simulation boundary conditions shows very similar results to the results for the displacement boundary conditions and the same trend in the sensitivity check of the meshing parameters. Therefore, the majority of these sensitivity analysis data is not repeatedly shown here again. The one worthy notice is that the stress boundary conditions show relatively large discrepancies for the sensitivity check on the model size. Specifically, the hoop stress at 0° using the stress boundary conditions hardly converges to the far-field

stress at the model boundary. This effect can be improved by increasing model size but it does not reduce to a satisfactory degree (Figure 4.7).

The comparison of the base model case using the three different boundary condition scenarios is shown in Figure 4.8. While the stress boundary conditions seem to provide the best solution at the borehole wall, especially for the hoop stress at 90° (Table 4.7), the discrepancies at distances larger than $r/R_w = 1.2$ become larger. The mean error and the standard deviation of the error of the hoop stress at 90° between $1.2 \leq r/R_w \leq 2$ for the stress boundary conditions are 1.04 MPa and 0.55MPa, respectively, compared to -0.53 MPa (mean error) and 0.13 MPa (standard deviation) for both displacement boundary conditions and for drilling simulation boundary conditions. Due to the similarity of the sensitivity analysis for all the three boundary conditions the same meshing guideline can be applied, and an optimized model according to the suggestion above can be obtained. In the optimized model the results for each boundary condition scenario are improved. In contrast to the base model, after optimization, the displacement boundary conditions and the drilling simulation boundary conditions now yield the smallest errors also at the borehole wall (Table 4.7) and are thus preferred over the stress boundary conditions. It should be noted that the drilling simulation boundary conditions increase the complexity of the modeling approach by their nature of implementation and thus displacement boundary conditions are recommended for wellbore stress analyses.

Table 4.7. Errors at the wellbore surface for the base model and the optimized model under the three types of boundary conditions.

Model	Numerical Errors at Borehole Wall (MPa)			
	$\sigma_{\theta\theta}$ at 0°	σ_{rr} at 0°	$\sigma_{\theta\theta}$ at 90°	σ_{rr} at 90°
Base				
Displacement	4.62	2.58	-8.23	0.10
Stress	3.11	2.71	-5.28	0.05
Drilling Sim	4.67	2.59	-8.23	0.10
Optimized				
Displacement	0.09	-0.29	-0.25	-0.50
Stress	0.40	0.30	0.60	0.51
Drilling Sim	0.08	-0.29	-0.25	0.50

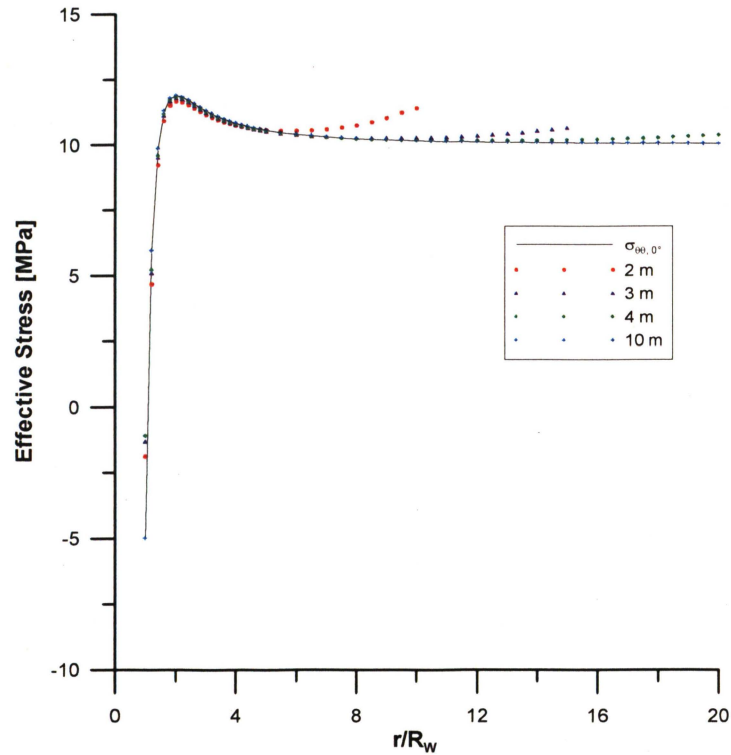


Figure 4.7. Hoop stress at 0° showing a great discrepancy near the far-field for the base model under the stress boundary condition.

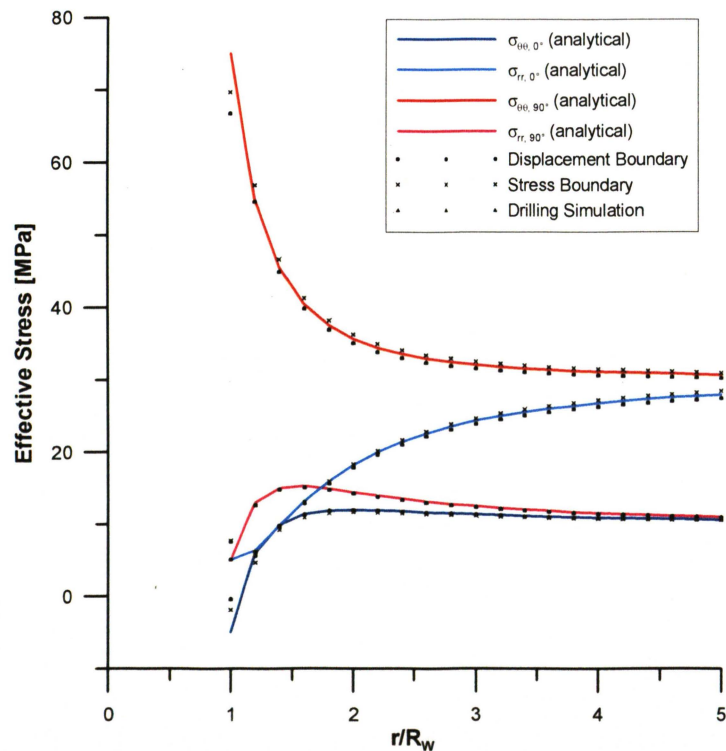


Figure 4.8. Base model using three boundary conditions and compared to the analytical solutions.

4.4. 3-D WELLBORE MODEL BUILT BASED ON 2-D WELLBORE MODEL

4.4.1. Comparison of the 3-D Base Model Results to the 2-D Base Model and the Analytical Solution. The 3-D model results show very similar results compared to the 2-D base model where it is generated from (Figure 4.9 and Table 4.8), and both have the same errors magnitudes in comparison to the analytical solution at the borehole wall. Thus, the 2-D wellbore model which serves as the borehole cross-section of the 3-D model can be used as a preliminary evaluation of the quality of the numerical results of the 3-D model to be built.

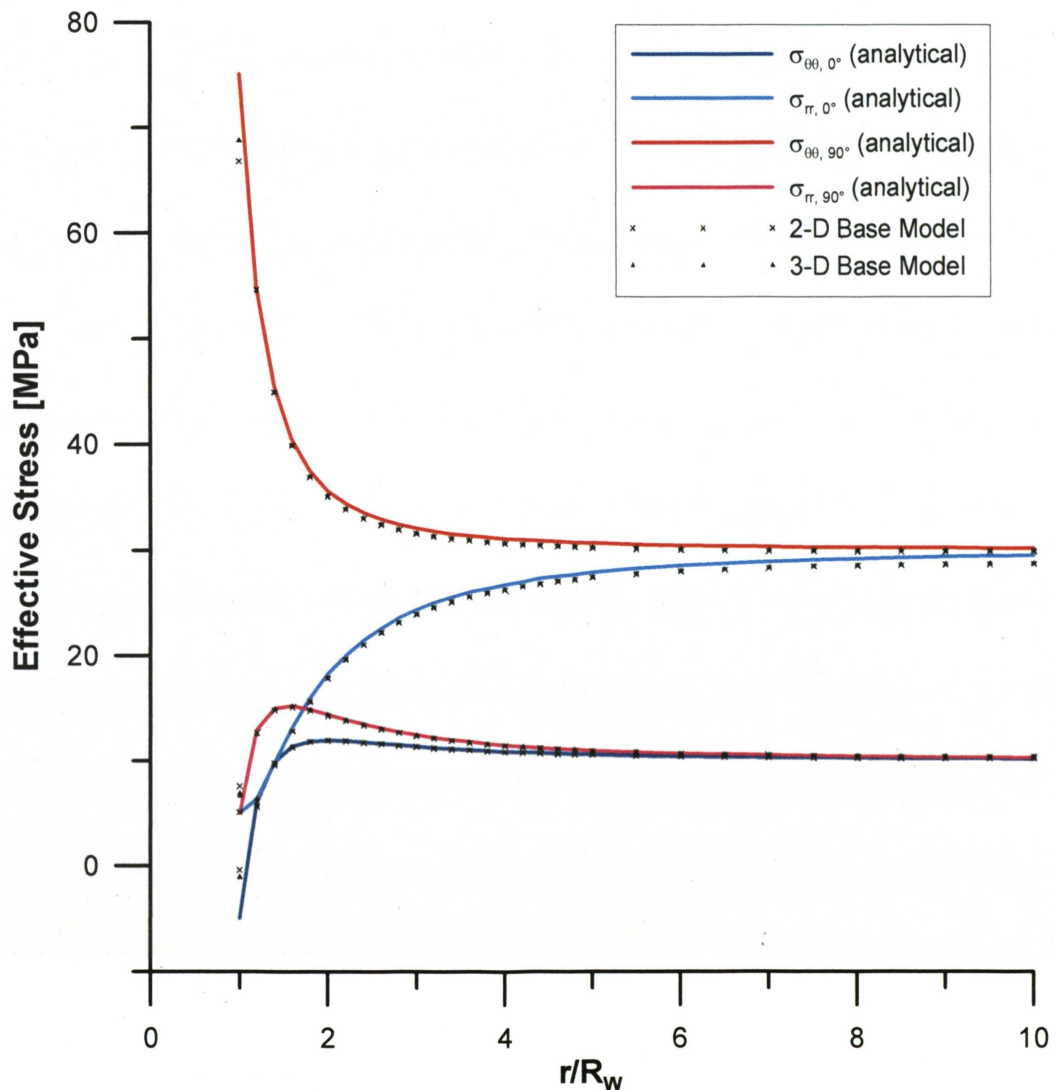


Figure 4.9. 2-D and 3-D Base models using displacement boundary conditions with comparison to the analytical solutions.

Table 4.8. 2-D and 3-D model results compared to analytical solutions

	Results at Borehole Wall (MPa)			
	$\sigma_{\theta\theta}$ at 0°	σ_{rr} at 0°	$\sigma_{\theta\theta}$ at 90°	σ_{rr} at 90°
Analytical	-5	5	75	5
2-D Base	-0.38	7.58	66.77	5.10
3-D Base	-1.09	6.90	68.73	6.63

4.4.2. Sensitivity Analysis of Model Height and Element Height. Different heights of the model and individual elements yield the same results as the base model, and thus identical errors compared to the analytical solutions (Tables 4.9 and 4.10). For a more complex material behavior or inclined wellbores, the element height is expected to have influence to the results due to the non-linear deformation of the model and the influence of the vertical stress in inclined wellbores [29].

Table 4.9. Sensitivity analysis of the model height for the 3-D model.

Model Height	Numerical Errors at Borehole Wall (MPa)			
	$\sigma_{\theta\theta}$ at 0°	σ_{rr} at 0°	$\sigma_{\theta\theta}$ at 90°	σ_{rr} at 90°
5m	4.62	2.58	-8.23	0.10
10m	4.62	2.58	-8.23	0.10
30m / 50m / 100m	4.62	2.58	-8.23	0.10

Table 4.10. Sensitivity analysis of the element height for the 3-D model.

Element Height	Numerical Errors at Borehole Wall (MPa)			
	$\sigma_{\theta\theta}$ at 0°	σ_{rr} at 0°	$\sigma_{\theta\theta}$ at 90°	σ_{rr} at 90°
0.5m	4.62	2.58	-8.23	0.10
1m	4.62	2.58	-8.23	0.10
5m / 10m	4.62	2.58	-8.23	0.10

4.4.3. Sensitivity Analysis of Element Type. For the sensitivity analysis of the element type, 1st order brick element(base model), 1st order brick reduced integration point element, and 2nd order brick element with full and reduced integration elements are studied (all listed elements are capable of handling pore pressure), which are referred to

as C3D8P, C3D8RP, C3D20P, and C3D20RP in ABAQUS™, respectively. The stresses at the nodes of the model are extrapolated from the results at the integration point where the stresses are initially computed in the FE model. Thus, theoretically, the nodal stresses are not as accurate as the stresses at the integration points, and a further decrease in number of integration points generates worse errors. At the borehole wall, the 2nd order brick element provides the smallest errors when compared to the other element types (Table 4.11). However, it should be noted that the processing time is about 20 times the processing time of the 1st order brick reduced-integration element.

Table 4.11. Sensitivity analysis of the element type for the 3-D model.

Element Type	Numerical Errors at Borehole Wall (MPa)			
	$\sigma_{\theta\theta}$ at 0°	σ_{rr} at 0°	$\sigma_{\theta\theta}$ at 90°	σ_{rr} at 90°
1st Brick	3.91	1.90	-6.27	1.63
1st Brick (Reduced)	6.40	0.53	-11.97	4.54
2nd Brick	0.28	-0.83	-0.20	1.67
2nd Brick (Reduced)	1.44	-0.43	-2.16	0.87

4.4.4. Optimized 3-D Wellbore Model. An optimized 3-D wellbore model is generated from the optimized 2-D wellbore mesh. The accuracy of the stresses at the borehole wall is greatly improved (Table 4.12). The largest error 0.51 MPa (for σ_{rr} at 90°) in the optimized 3-D model is very similar to the largest error 0.50 MPa in the optimized 2-D model .

Table 4.12. 3-D and 2-D optimized model results compared to the analytical solutions

	Results at Borehole Wall (MPa)			
	$\sigma_{\theta\theta}$ at 0°	σ_{rr} at 0°	$\sigma_{\theta\theta}$ at 90°	σ_{rr} at 90°
Analytical	-5	5	75	5
2-D Optimized	-4.91	4.71	74.75	5.50
3-D Optimized	-4.94	4.70	74.79	5.51

5. DISCUSSION

5.1. 2-D MODELS USING DISPLACEMENT BOUNDARY CONDITIONS

The numerical study presented in this paper shows that, considering the general availability of numerical modeling tools such as the finite element (FE) method, care has to be taken when these methods are applied for wellbore stress analysis. It is obvious that for the case of a homogeneous, isotropic, linear elastic material the analytical solution provides the accurate solution and numerical analysis is not necessary. However, many applications for wellbore stability or hydraulic fracturing require composite materials (e.g. cementing analysis; [30]) where analytical solutions do not exist. Therefore, numerical wellbore stress analysis for a homogeneous, isotropic, linear elastic material provides an excellent opportunity to test the influence of the various discretization parameters on the existing analytical solution [3] and to provide conclusions for meshing and model optimization requirements for all types of wellbore stress analyses. A variety of studies have shown that the accuracy of results of FE studies are highly dependent on discretization approaches and parameters [31, 32, 33]. Even if errors of the modeled results are within 1 to 3 MPa [10], these should be taken seriously, otherwise the subsequent study based on the modeled results might be questionable.

This study shows that the most prominent improvement on the accuracy of the modeled result is obtained by using 2nd order elements. The -8.23 MPa error of the hoop stress at 90° in the base model using the displacement boundary is decreased to around 1 MPa by merely changing the element type with other modeling parameters fixed, and at no cost to the increase of the numbers of the elements, although more nodes are used. In the sensitivity analysis, the increase of the radial mesh density in the near wellbore region reduces the error to around 5 MPa, and its influence marginally diminishes. Thus choosing 2nd order elements has the highest priority before the increase of mesh density.

In the context of the significance of the numerical errors, it should be noted that the FE method inherently introduces errors as it is a method of approximation [8]. This becomes most evident when comparing the stress results at the borehole wall, where the numerical model yields the largest error. One has to understand that the FE method calculates stresses at the element integration point using Gaussian integration [34], which

is situated inside the element (Figure 5.1) and thus cannot reproduce the absolute exact result at free surfaces like the borehole wall. To compare FE model stresses to the analytical solution the element stresses from the integration points have to be extrapolated to the nodal coordinates (Figure 5.1). This procedure generally provides very accurate agreements for nodes attached to 4 elements but at the free surface of the borehole wall an error is introduced. Here, the stress changes rapidly and the stress at this node is extrapolated from the two integration points inside the formation only. This extrapolation will always return a non-zero stress value for the radial stress (if no fluid pressure is applied) and thus cannot obey the rule that normal stresses do not exist at a free surface.

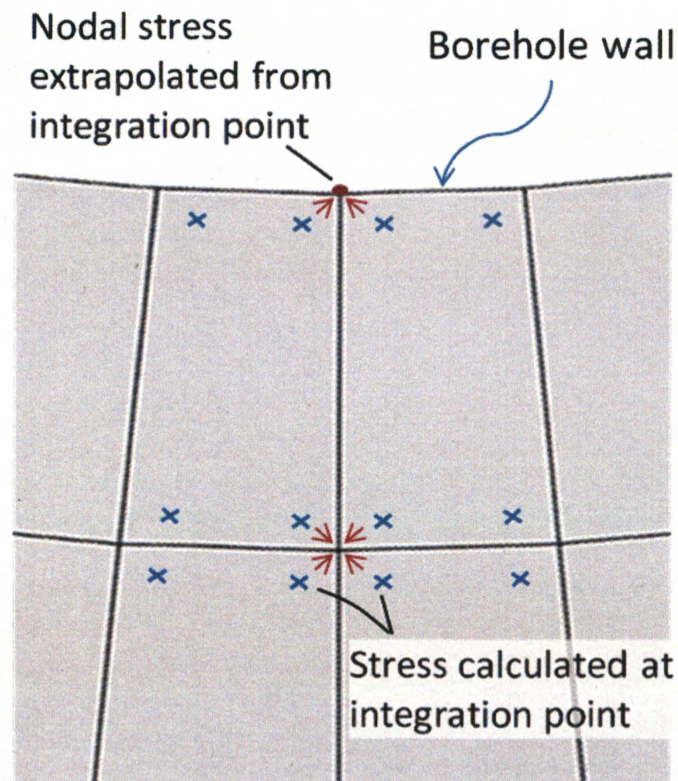


Figure 5.1. Stresses at the element integration points extrapolated to the nodal positions introducing greater errors, especially near the borehole wall.

5.2. COMPARISON OF MODELS USING DIFFERENT BOUNDARY CONDITIONS

The displacement and drilling simulation boundary conditions produce almost identical results and yield smaller errors than the stress boundary conditions. Displacement boundary conditions are a numerically less complicated for wellbore modeling because the drilling simulation boundary conditions require an additional initial pre-stressing procedure. For a 3-D wellbore model, if the model is to simulate non-uniform stresses along different depths, then using the drilling displacement boundary conditions is a better option since it is more manageable and precise to apply the pre-stressing to the model with the given in-situ stresses, rather than converting them to boundary displacement at varied depths of the model boundary.

5.3. UTILIZATION OF 3-D MODELS

In general, the 3-D model is better suited for a comprehensive wellbore stability analysis, e.g. considering directional drilling, complex geological structures, material anisotropy, hydraulic fracturing, etc [30]. From the presented analysis of a vertical wellbore it can be inferred that stress around the borehole is majorly determined by how the mesh is organized in the well opening plane.

The need for 3-D models becomes evident when considering the vertical model size and mesh resolution. While, as presented here for a vertical wellbore, the vertical dimension model parameters have no influence on the results (even though those elements all have a very high aspect ratio, from 50 up to around 1000), it is crucial to optimize these parameters for inclined wellbores. For inclined wellbores the hoop stress and hence the maximum and minimum tangential stress at the borehole wall, which are responsible for borehole failure, are directly dependent on the vertical stress [29]. It should be noted that the general validity of the presented mesh optimization is fully granted for inclined wellbores when the coordinate system is chosen appropriately (i.e. borehole coordinate system).

5.4. IMPLICATIONS OF SAFE MUD WEIGHT PREDICTION

In order to demonstrate the significance of the numerical errors for wellbore stability applications we predict the safe mud weight window for the base model, the optimized model, and for the analytical solution under three different stress regimes: normal or extensional faulting (NF), strike-slip (SS) faulting, and compressional or reverse faulting (RF) regime. It should be noted again that the evaluation of an appropriate failure criterion for wellbore stability analyses is beyond the scope of this thesis and that each failure criterion is affected differently by the numerical errors. We use the Mohr-Coulomb failure criterion as the most conservative [16] criterion for this analysis to point out the general implications for wellbore stability.

The magnitudes of the horizontal stresses are based on a vertical well at 2000 m depth with a hydrostatic pore pressure of 19.62 MPa (i.e. using a pore fluid density of 1g/cm^3) and an overburden stress of 44.15 MPa (i.e., using an overburden rock density of 2.25g/cm^3). The rock formation is based on a typical sandstone, which has a cohesion of 5.10 MPa, a friction angle of 33° and a Poisson's ratio of 0.25 [35]. Table 5.1 lists the stress magnitudes for the different regimes applied for the far-field stresses.

Table 5.1. State of stress for the different stress regimes applied to the wellbore models.

Stress Regime	σ_v (MPa)	σ_H (MPa)	σ_h (MPa)
NF	44.15	35.97	27.80
SS	44.15	52.97	33.11
RF	44.15	66.22	55.18

The numerical results of the hoop and radial stresses at the borehole wall for the base (non-optimized) model and the optimized model are compared to the analytical solution, and the errors for each stress regime are shown in Table 5.2. The results for the base model show that for all stress regimes considered the highest errors occur at the locations prone to borehole breakouts, i.e. for the hoop stress at 90° (-6.42 MPa for NF, -10.93 MPa for SS and 10.78 MPa for RF). The stress errors for the radial stress at 0° and 90° and the hoop stress at 0° are less, but still significant. In comparison, the errors obtained from the optimized model are less than 0.65MPa for all locations.

Table 5.2. Stress errors at the borehole wall of the base model and optimized model under the three stress regimes.

Model	Numerical Errors at Borehole Wall (MPa)			
	$\sigma_{\theta\theta}$ at 0°	σ_{rr} at 0°	$\sigma_{\theta\theta}$ at 90°	σ_{rr} at 90°
Base				
NF	-1.17	3.38	-6.42	2.36
SS	0.43	5.07	-10.93	2.87
RF	-5.65	6.14	-10.78	4.77
Optimized				
NF	-0.13	0.06	-0.25	0.38
SS	-0.12	-0.05	-0.38	0.65
RF	-0.25	0.20	-0.45	0.63

To accurately predict the safe mud weight window, the optimized 2-D model using displacement boundary conditions is used. The results show that the collapse pressure gradient and the breakdown pressure gradient for the optimized model have a maximum error of -0.03 specific gravity (s.g.) or -0.25 ppg. This error is within the practical limit of mud density control [36].

Table 5.3. Predicted safe mud weight window using the Mohr Coulomb failure criterion.

Stress Regime	Safe Mud Weight Window (s.g.)		
	Analytical	Optimized	Base
NF	1.26 – 1.55	1.24 – 1.54	1.09 – 1.49
SS	1.76 – 1.83	1.73 – 1.82	1.52 – 1.85
RF	1.99 – 4.19	1.96 – 4.18	1.68 – 4.01

However, if the safe mud weight window for the base (non-optimized) model is predicted (for all three stress regimes), the errors become significant. For the collapse pressure gradient the model yields a much lower collapse pressure compared to the analytical solution. With errors of -0.17, -0.24, and -0.31 s.g. (or 1.4, 2.0, and 2.6 ppg) for NF, SS, and RF regimes, respectively, this would lead to an over-optimistic prediction for the mud weight. If these errors from the modeling were neglected, mud weights causing borehole breakouts might be chosen.

This is most noticeable for the strike-slip regime where vertical wells represent the least stable well direction. For the example case the analytical solution shows that the safe mud weight window is very narrow (1.76 to 1.83 s.g. or 14.67 to 15.23 ppg), while the non-optimized model results predict a mud weight window of 1.57 to 1.85 s.g. or 13.05 to 15.43 ppg. This clearly overestimates the range of actual applicable mud weights and a stable borehole cannot be guaranteed.

The breakdown pressure is determined by the hoop stress at 0° . Though the base model only yields an error of 0.02 s.g. of the breakdown pressure gradient in the strike-slip stress regime, the breakdown pressure for the normal faulting and reverse faulting regime shows significant errors of -0.06 and -0.18 s.g. (or 0.5 and 1.5 ppg), respectively. Such errors are of less importance for the reverse faulting regime because the safe mud weight window is rather wide. However, for hydraulic fracturing applications the error accounts for an underestimation of 1.5 ppg of the fracture gradient.

Although only the Mohr-Coulomb failure criterion is used in the wellbore stability analysis, this study shows that the choice of boundary conditions and meshing parameters has crucial implications to the applications of wellbore stress analyses.

5.5. APPLICATION OF THE WELLBORE MODEL ON GEOLOGICAL STORAGE OF CO₂ IN A GENERIC RESERVOIR

5.5.1. Geomechanical Modeling for Carbon Storage. The Greenhouse gas effect is widely regarded as the main cause of global warming [37]. Carbon dioxide represents the largest contribution from human activities. To prevent environmental damages from releasing CO₂ into the atmosphere, carbon capture and storage has been very an important topic in recent research projects. The current options for CO₂ storage are underground geological storage, ocean storage and mineral carbonation storage. For geological storage, depleted oil and gas reservoirs, coal formations and saline formations can be used. Liquid-phase CO₂ provides an efficient use of the underground storage space in the pores of sedimentary rocks. Carbon dioxide can be stored underground by trapping below an impermeable caprock formation; dissolution in the formation fluids; and adsorption as organic matter in coal and shale. The risk of CO₂ leakage through the cap

rock and fracture networks has been an issue in successful sequestration of the CO₂. Assessment of cap rock stability, fracture generation and reactivation and wellbore integrity due to injection related pore pressure increase becomes of major interest. Geomechanical modeling of the underground storage will help to find suitable conditions for possible CO₂ sequestration sites.

5.5.2. Reservoir-Scale Model and Wellbore-Scale Model. In the context of CO₂ sequestration anticline structures become prime targets for geologic sequestration of CO₂ [37] and thus risks associated to wellbore stability in this geological structure are of importance. Accordingly, a generic 2-D reservoir scale model comprising a multi-layer anticline structure is presented [38; Figure 5.2] to model the in situ stresses in the reservoir layer under the compressive forces from the far-field stresses, and the optimized 3-D wellbore model of this present study is used to address wellbore integrity and optimal wellbore placement in the geological structure. For the generic anticline reservoir wellbore integrity is studied at different injection locations in the anticline structure (i.e. crest, limb and syncline) before and after CO₂ injection.

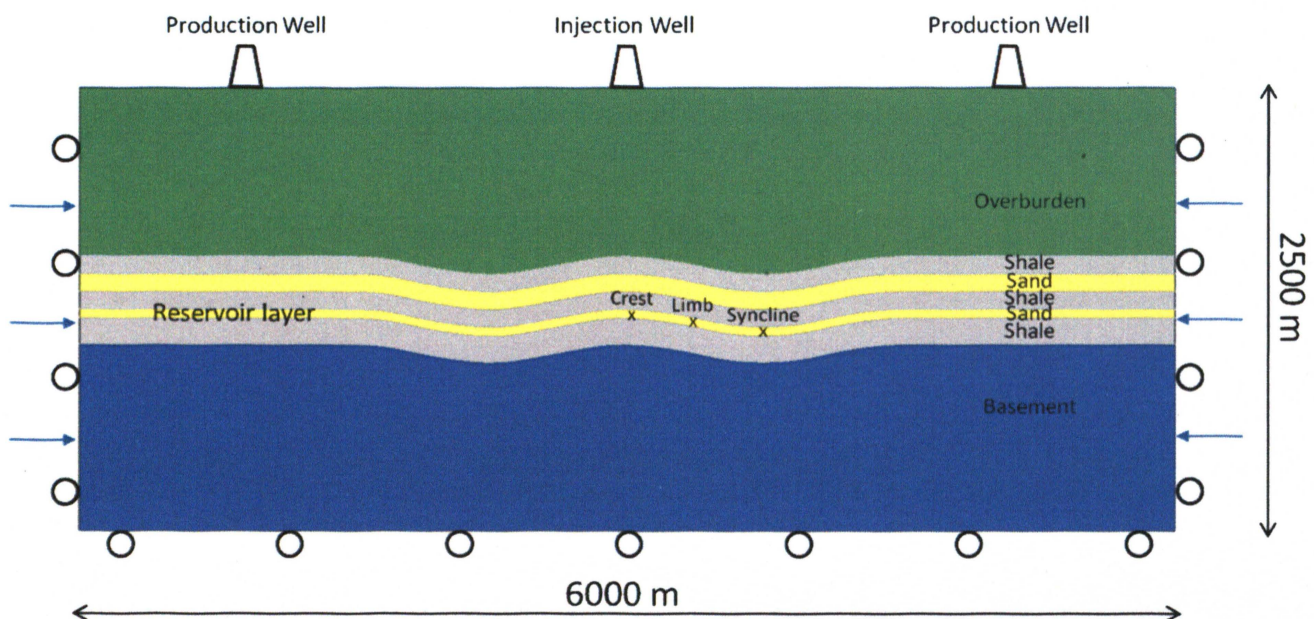


Figure 5.2. Reservoir model of anticline for CO₂ storage.

The anticline structure of the reservoir model is subjected to three different stress regimes, reflecting extensional, strike-slip and compressional stress regimes. Plane strain finite element analysis is used in the 2-D reservoir scale model, and thus three principal stress components can be simulated in 2-dimensions. The k ratio, defined by the ratio of the mean horizontal to the vertical stress, is used to determine the relationship among the horizontal stresses and vertical stress for the three stress regimes. k ratios of 0.5, 1, and 1.15 are chosen for extension, strike-slip, and compression, respectively. The vertical stress is calculated at a depth of 1350m, and then the corresponding horizontal stresses can be obtained from the k ratio for each stress regime. The detailed data of the reservoir structure and material properties is listed in the Appendix.

The anticline structure is modeled as a flexural-slip fold system where layer parallel slip between the folded strata is allowed. To simulate the decoupling of the bedding planes, the friction coefficient between the layers in the 2-D reservoir model is studied for settings of $\mu=0.05$ and $\mu=0.8$.

By using the in-situ effective stress modeled from the reservoir scale models with hydrostatic pore pressure, 3-D wellbore models for wellbore placement and orientation at different locations, i.e. crest and limb of the anticline and the syncline, of the geological structure are studied (Figure 5.2). The 3-D wellbore model with the optimized mesh presented in the previous chapters is utilized.

5.5.3. Wellbore Stability of a Vertical Well in the Reservoir Layer. In the case of a vertical wellbore, the wellbore stability during drilling operation can be achieved only in the extensional region case. For the first scenarios presented the different layers of the anticline structure are decoupled, as represented by a low coefficient of friction between them ($\mu=0.05$). Figure 5.3 shows the safe mud weight window for the extensional regime for the different drilling locations at the crest, the limb, and the syncline of the geological structure. Drilling through the crest has the narrowest safe mud window among the three locations, and the safe mud weight window is narrower at the bottom (an interval of 0.5 ppg) of the reservoir than at the top (an interval of 0.9 ppg). This is due to the distribution of stresses within a fold structure

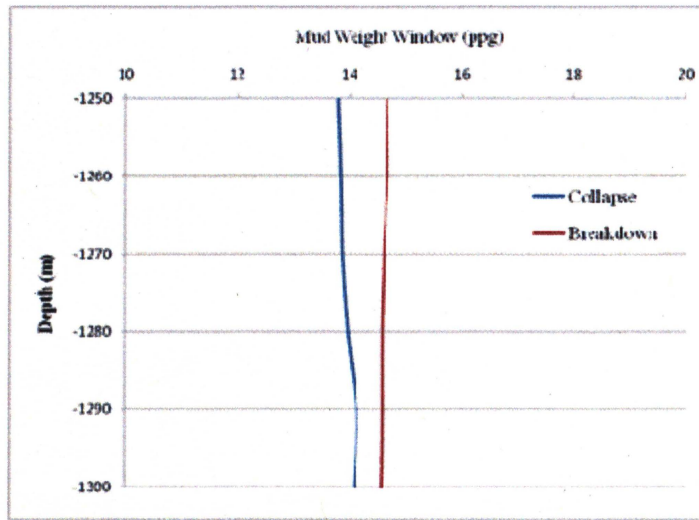
where higher compressive stresses are at the bottom of the crest zone. At the syncline, where the compressive stress is higher at the top than at the bottom of the layer, a larger interval of the mud weight window can be obtained when it gets deeper to the bottom of the syncline layer. At the limb, the state of stresses shows that the maximum principal stress is in the direction of the bedding plane thus the vertical wellbore can be regarded as an “inclined” wellbore with respect to the bedding plane of 11.8° . It can be observed from Figure 5.3 that the difference for the collapse pressure is not large for all three locations. However the breakdown pressure shows significant differences and a larger safe mud weight window can be achieved. Figure 5.3(b) shows that the safe mud weight window at the limb, i.e. 1.76 ppg, is the widest among the three locations.

For the strike-slip and compressional regime the collapse pressure exceeds the breakdown pressure and thus no appropriate drilling fluid can be used to keep the borehole stable (Figures 5.4 and 5.5). In such cases any mud density chosen will cause borehole breakdown, drilling-induced tensile failure, or both. Among the three stress regimes, the compressional model is most prone to breakouts because of the largest difference in the maximum and minimum horizontal stresses.

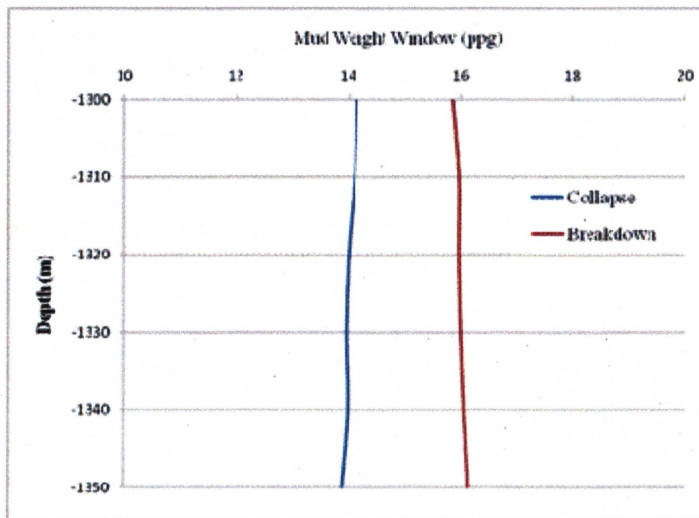
In the case of a stronger coupling between the layers ($\mu = 0.8$), the models exhibit a different stress distribution than the models with a low friction coefficient. These effects are more profound in the compressional regime due to the high maximum horizontal stress. Due to the strong coupling the various layers act almost as a singular unit and the observation of lower compression at the top of the crest compared to high compression at the bottom of the crest cannot be validated for this case. However, the reservoir layer is thin enough (50m) such that the in-situ stresses in the reservoir for the two friction coefficients are of similar order of magnitude such that no improvement to wellbore instability issue can be found in the reservoir layer (Figure 5.6).

A wellbore stability analysis for the complete depth range of a vertical well through the crest of the anticline under the extensional stress regime shows interesting implications for the safe mud weight window (Figure 5.7). The mud weight window shows step function since the stress distribution is not continuous from layer to layer due to the material heterogeneities. In the decoupling model, the layers are allowed to slip between each other and experience buckling behavior, resulting in higher compression at

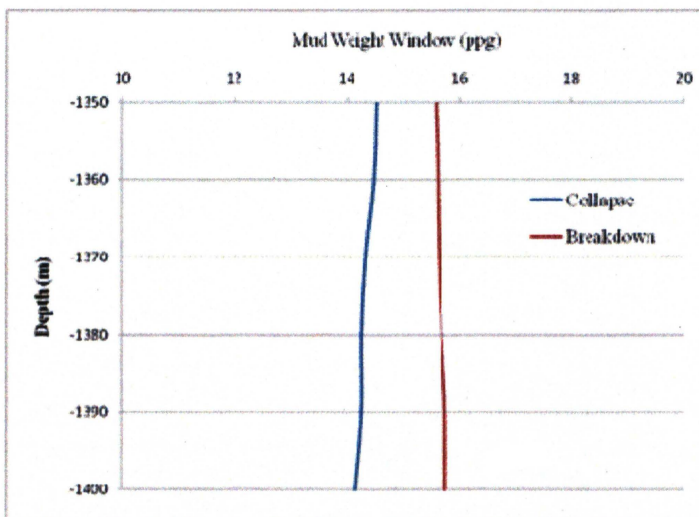
the top of the fold (Figures 5.8). Nevertheless, in the coupling models the slip movements between layers are limited that it shows reverse results: lower compression at the top of the fold, and higher compression at the bottom (Figures 5.9). It should be noted that the change in stress along the depth in the layers of the coupling models are not as obvious as in the decoupling models. The stress distribution in the reservoir model for the decoupling and the coupling cases are in an opposite manner in each layer such that the model of $\mu= 0.05$ has a wider safe mud weight window at the top of each layer, while the model of $\mu= 0.8$ has a narrower safe mud weight window at the top of each layer. These effects in the decoupling and coupling models are more remarkable in the compressional stress regime since the S11 is the highest among the three stress regime.



(a)

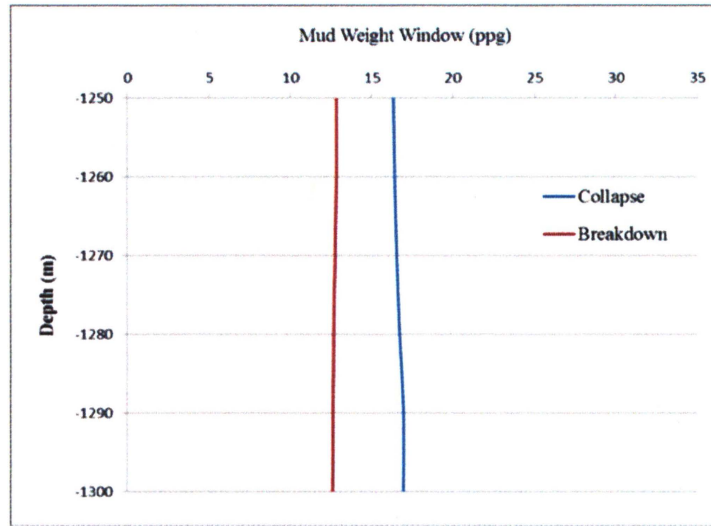


(b)

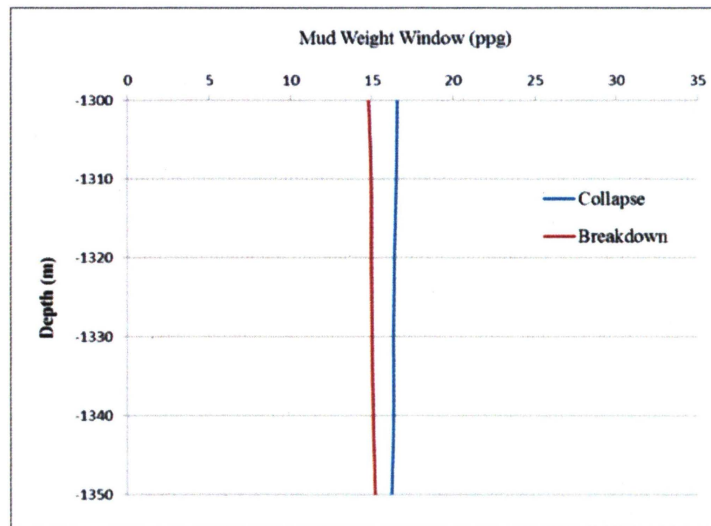


(c)

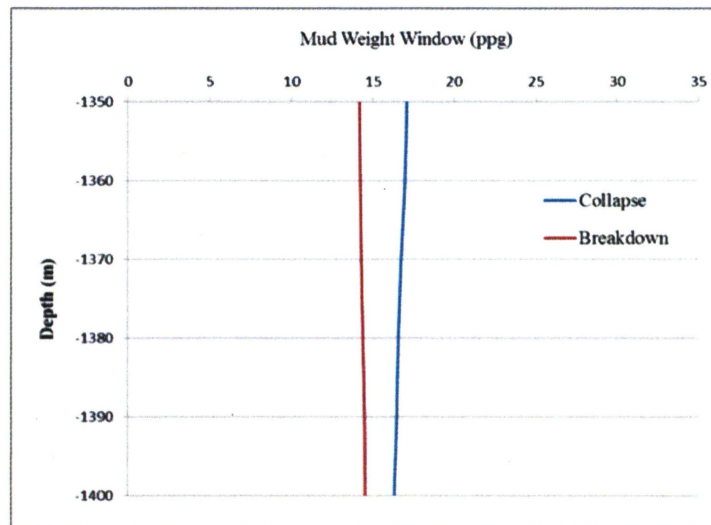
Figure 5.3. Mud weight windows of the reservoir layer of vertical well at (a) crest, (b) limb, and (c) syncline under the extensional stress regime.



(a)

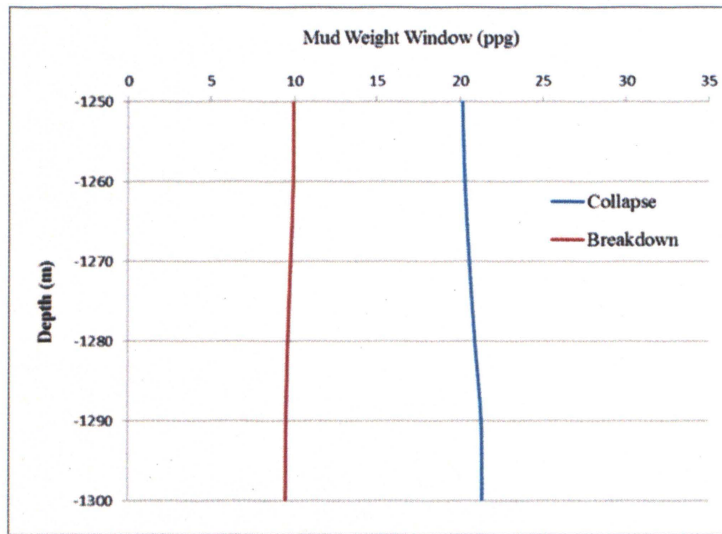


(b)

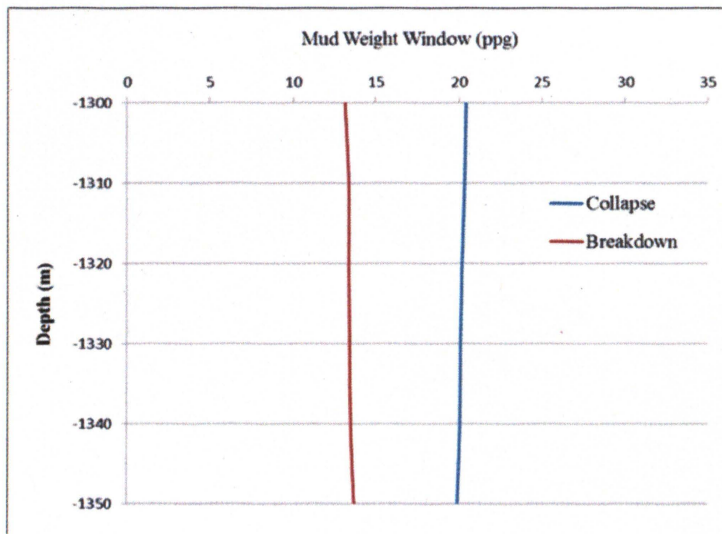


(c)

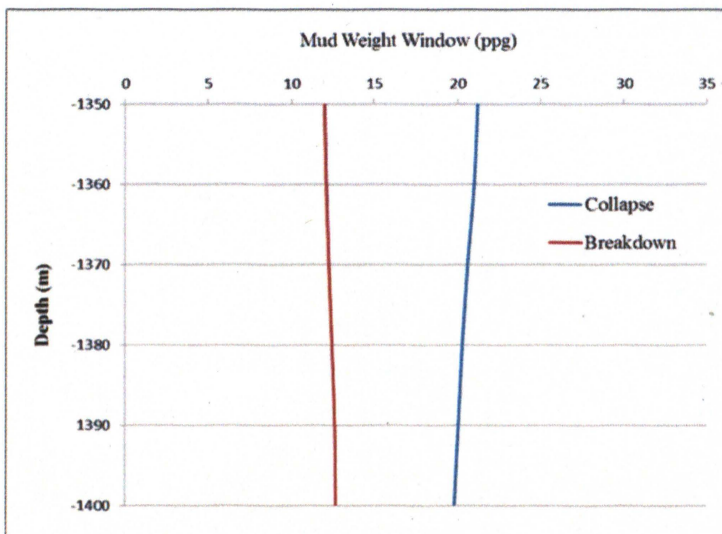
Figure 5.4. Mud weight windows for the reservoir layer of vertical wells at (a) crest, (b) limb, and (c) syncline under the strike-slip stress regime.



(a)



(b)



(c)

Figure 5.5. Mud weight windows of vertical wells at (a) crest, (b) limb, and (c) syncline under the compressional stress regime.

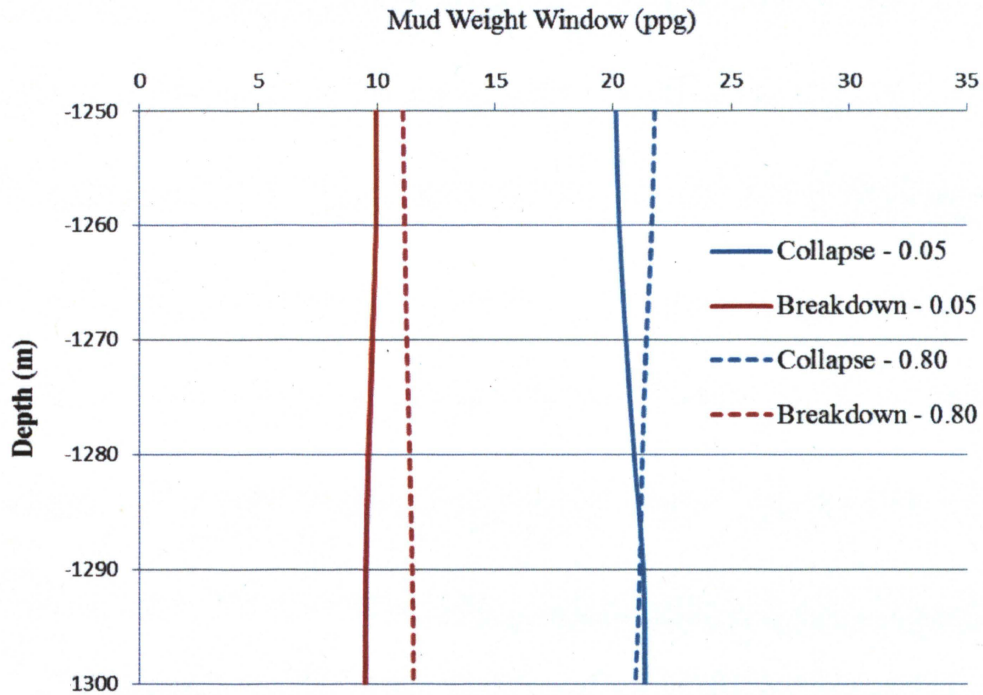


Figure 5.6. Mud weight window of the vertical well at the crest of the anticline under the compressional stress regime. No stable wellbore can be sustained for both coefficients of friction (0.05 & 0.8).

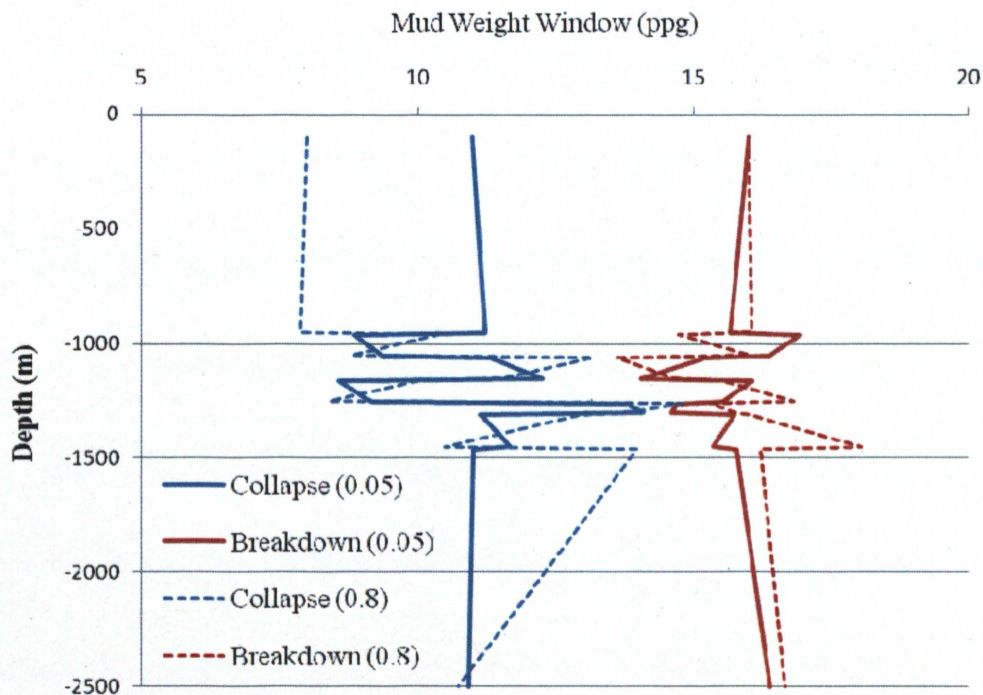
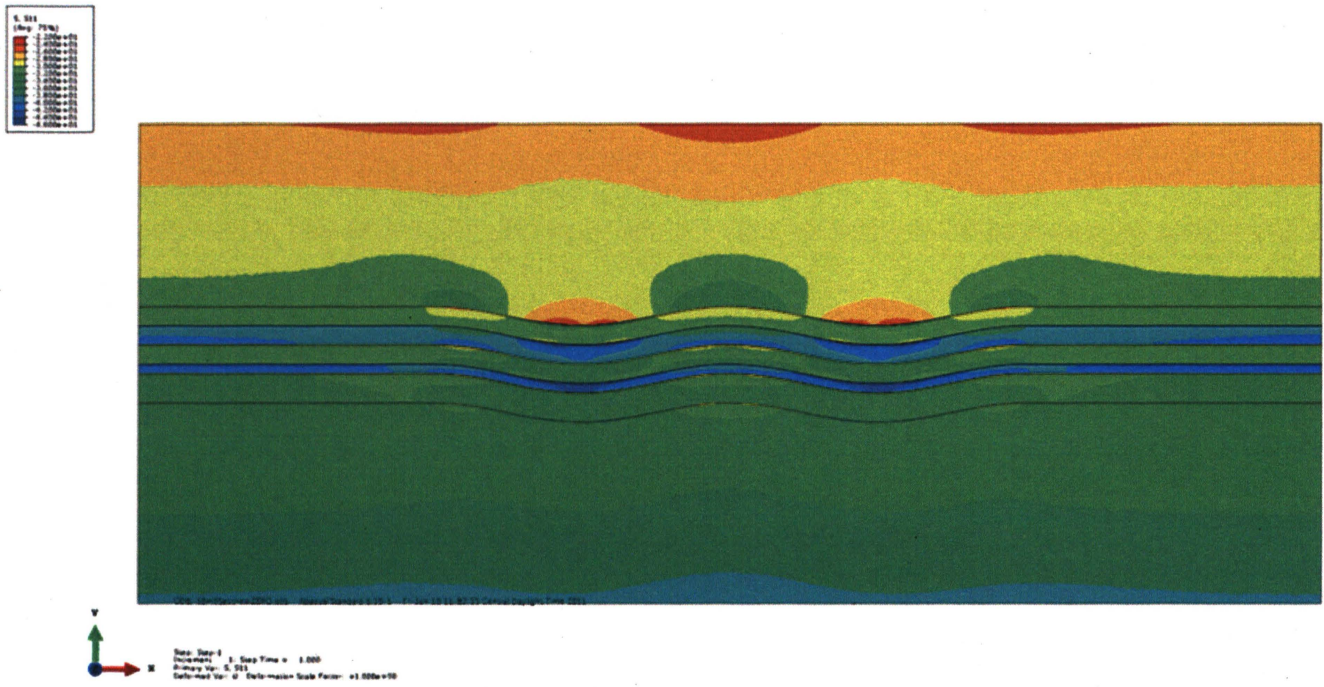
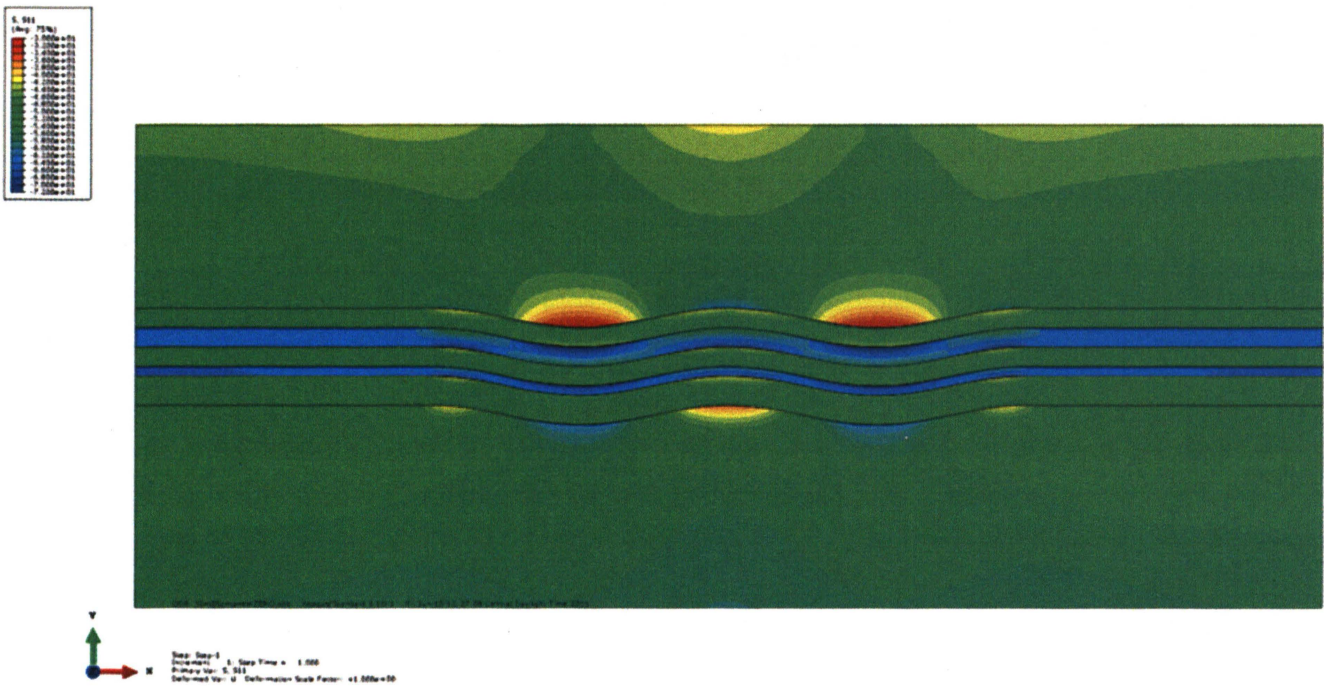


Figure 5.7. Mud weight window of the vertical well at the crest of the anticline for the total depth under the extensional stress regime.

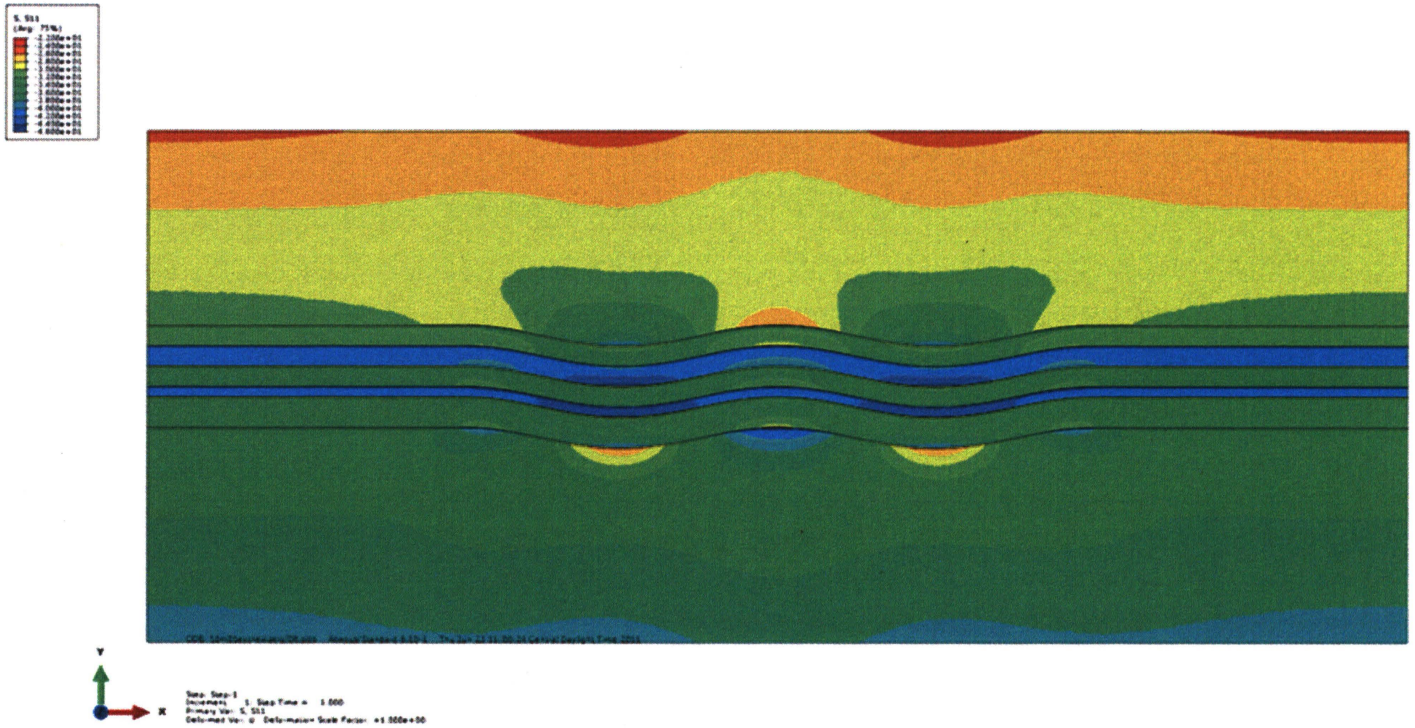


(a)

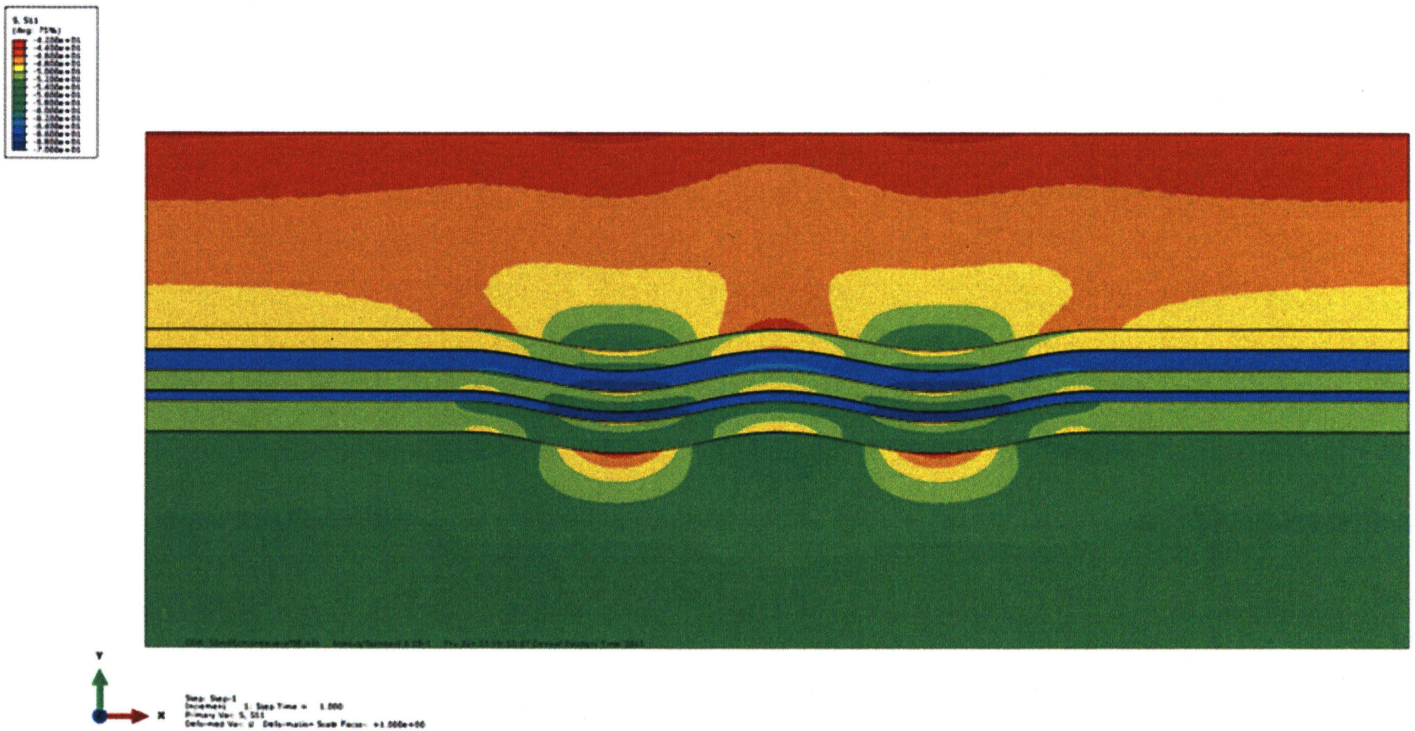


(b)

Figure 5.8. Reservoir models of coefficient of friction 0.05 under (a) extensional stress regime and (b) compressional stress regimes.



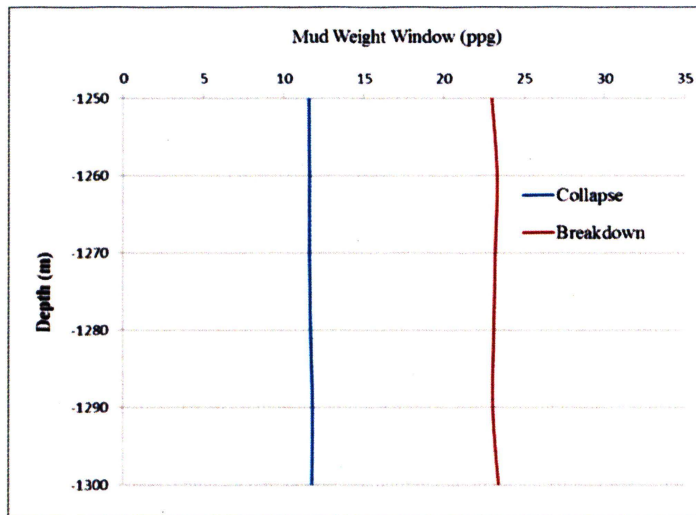
(a)



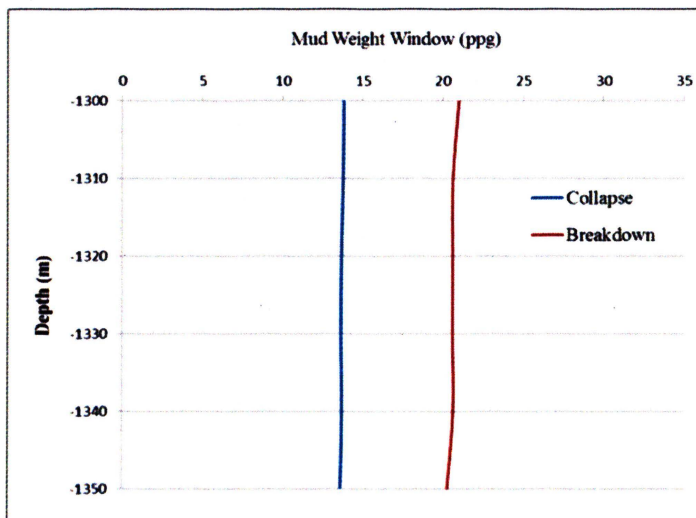
(b)

Figure 5.9. Reservoir models of coefficient of friction 0.80 under (a) extensional stress regime and (b) compressional stress regimes.

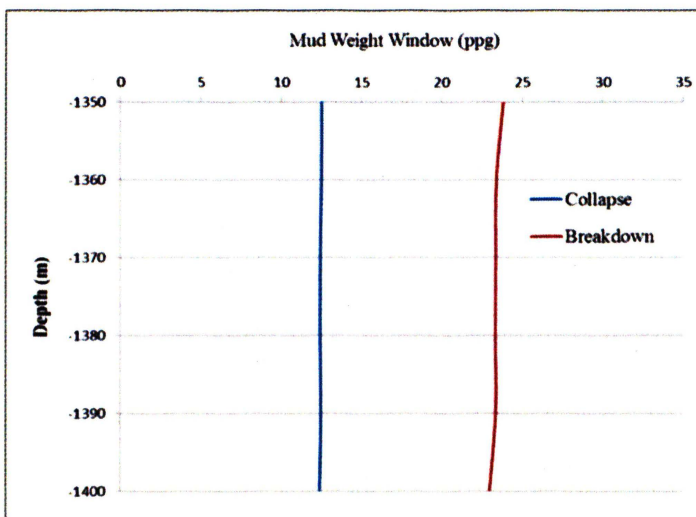
5.5.4. Wellbore Stability of Inclined Well in the Reservoir Layer. For the exemplary cases presented, vertical wells are not stable under the strike-slip and compressional stress regime, regardless of the drilling locations. To ensure stable wellbore conditions during drilling, inclined wells of 45 degree and 90 degree (horizontal) to the azimuth of σ_H are investigated for all three stress regimes at each location. Both inclination angles under all three stress regimes can provide stable wellbore at all three locations. Figures 5.10 and 5.11 show that for the 45°-inclined wellbore the breakdown pressure becomes larger than the collapse pressure and that the mud weight window becomes large enough to ensure stable drilling through the reservoir layer. Inclination of the wellbore decreases the maximum normal stress acting on the borehole axis along with the generation of shear stress on the x-z plane. Accordingly the hoop stress at 90° is decreased resulting in a lower collapse pressure while the hoop stress at 0° is increased resulting in a higher breakdown pressure. It is important to note that while vertical wellbores do not account for stable drilling conditions in the strike-slip and the compressional stress regime, inclined wellbore provide solutions for stable drilling conditions. Figures 5.12 shows the safe mud weight window for a horizontal well at crest under three stress regimes. The lower limit of the mud weight window is governed by the pore pressure instead of collapse pressure to prevent a kick.



(a)

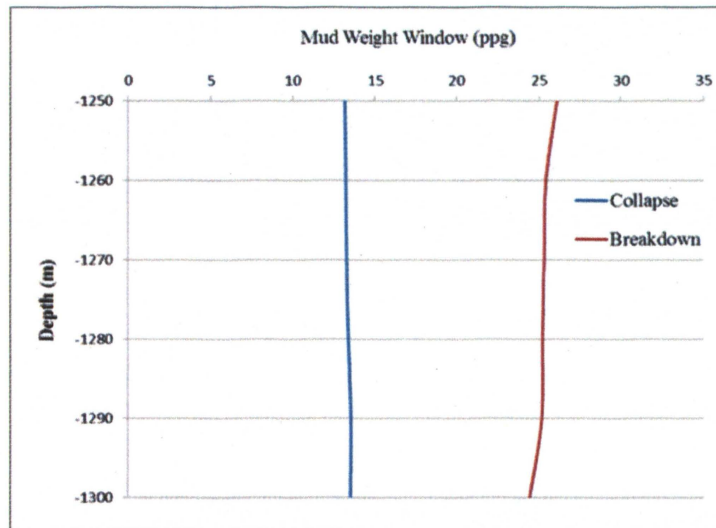


(b)

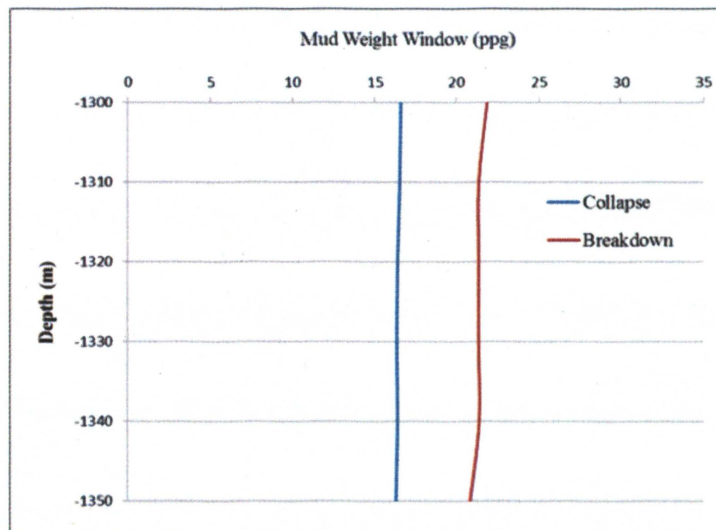


(c)

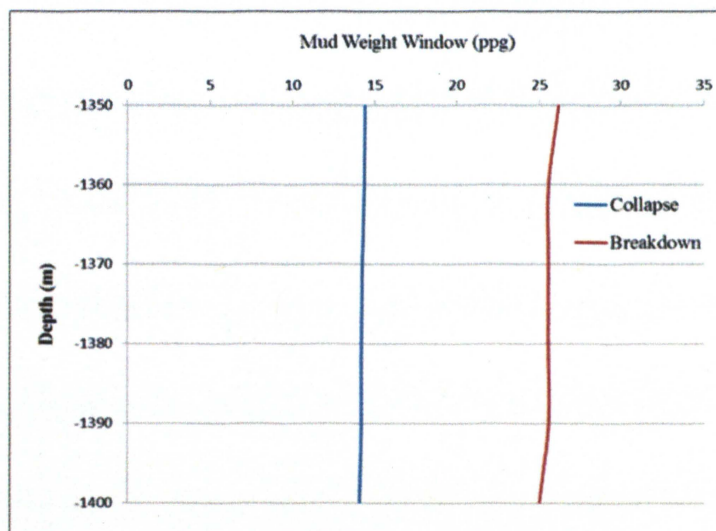
Figure 5.10. Mud weight windows of a 45°-inclined well (with respect to σ_1) at (a) crest, (b) limb, and (c) syncline of the reservoir layer under the strike-slip stress regime.



(a)

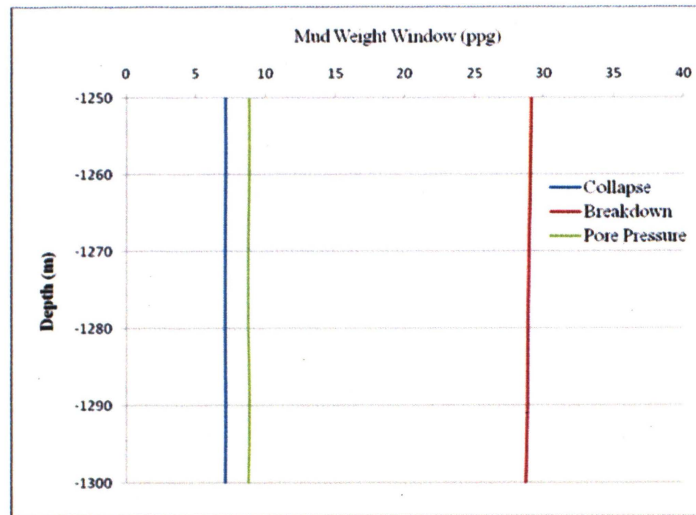


(b)

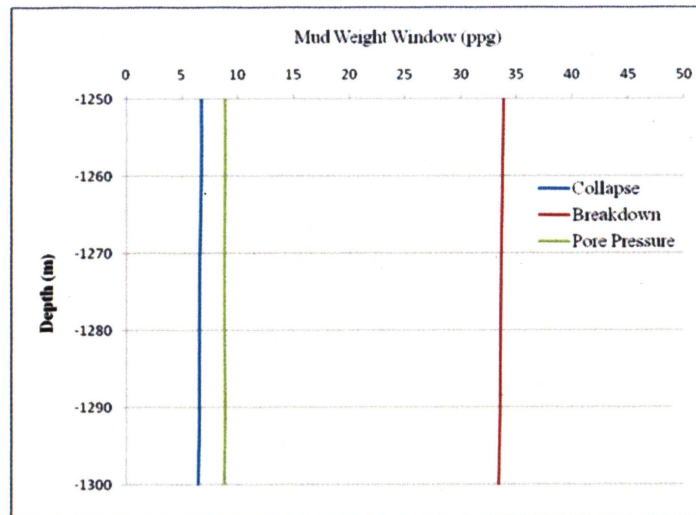


(c)

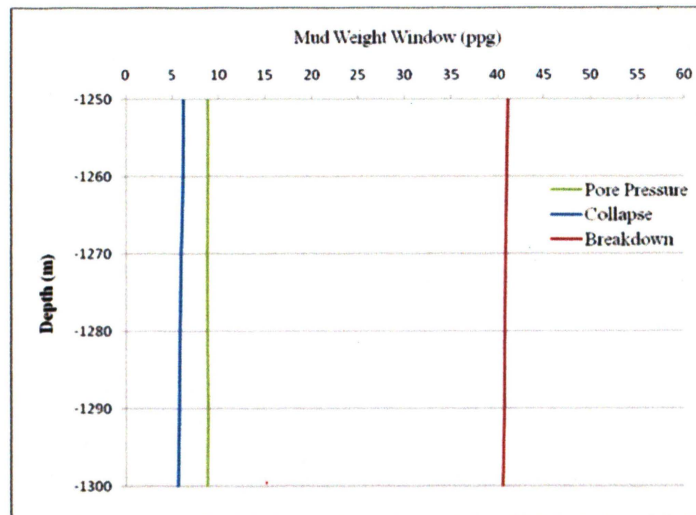
Figure 5.11. Mud weight windows of 45°-inclined well at (a) crest, (b) limb, and (c) syncline of the reservoir layer under the compressional stress regime.



(a)



(b)



(c)

Figure 5.12. Mud weight windows of horizontal well at crest of the reservoir layer under (a) extensional, (b) strike-slip, and (c) compressional stress regimes.

5.5.5. CO₂ Sequestration Model. CO₂ injection into the reservoir layer increases the fluid pressure over time, and thus the effect of that pressure increase on wellbore integrity is studied. The CO₂ injection is modeled using a reservoir simulation model (ECLIPSE™) which shares the same discretization as the FE model. The reservoir simulation is necessary because the reservoir simulator can better model the multi-component, multi-phase fluid flow in porous media than the geomechanical simulator. The reservoir is initially fully saturated with water, and CO₂ is injected at the crest of the anticline. Two water production wells are set up 2.5 km away from the injection well. The CO₂ injection rate is 5000 m³/day, and the water production rate is 7 m³/day for each production well. A coupling procedure [39] is used for the CO₂ injection model: the reservoir simulator Eclipse is used to retrieve the pore pressure after a period of injection time, then the pore pressure is applied to the geomechanical model for wellbore integrity analysis.

It should be noted that the presented wellbore integrity analysis of the CO₂ injection scenario is valid for an open-hole analysis only, since the FE model utilizes homogeneous elastic material without simulating a composite wellbore completion including cement and casing.

5.5.6. Wellbore Integrity after CO₂ Injection. From the wellbore stability analysis for a vertical well discussed in the previous paragraph, a stable vertical well can only be maintained in the extensional case. For an exemplary case of CO₂ injection at the crest of the anticline, wellbore integrity is investigated for the open-hole section in the reservoir layer. At the first day of CO₂ injection, the bottom hole pressure of the CO₂ is at 15.2 MPa to maintain the 5000 m³/day injection rate. However, the critical collapse pressure for this openhole section is 21.57 MPa, which is higher than the bottom hole pressure such that borehole breakouts will occur (Figure 5.13). It is clear that for a vertical well, injection at an open-hole section of the wellbore is not feasible because the bottom hole pressure is not high enough to sustain the borehole wall. No further injection can be done since wellbore integrity cannot be maintained in the open-hole section. This study does not cover a completion well for the wellbore integrity analysis because a

completed well for the evaluation of CO₂ leakage mechanism is not available yet at this time.

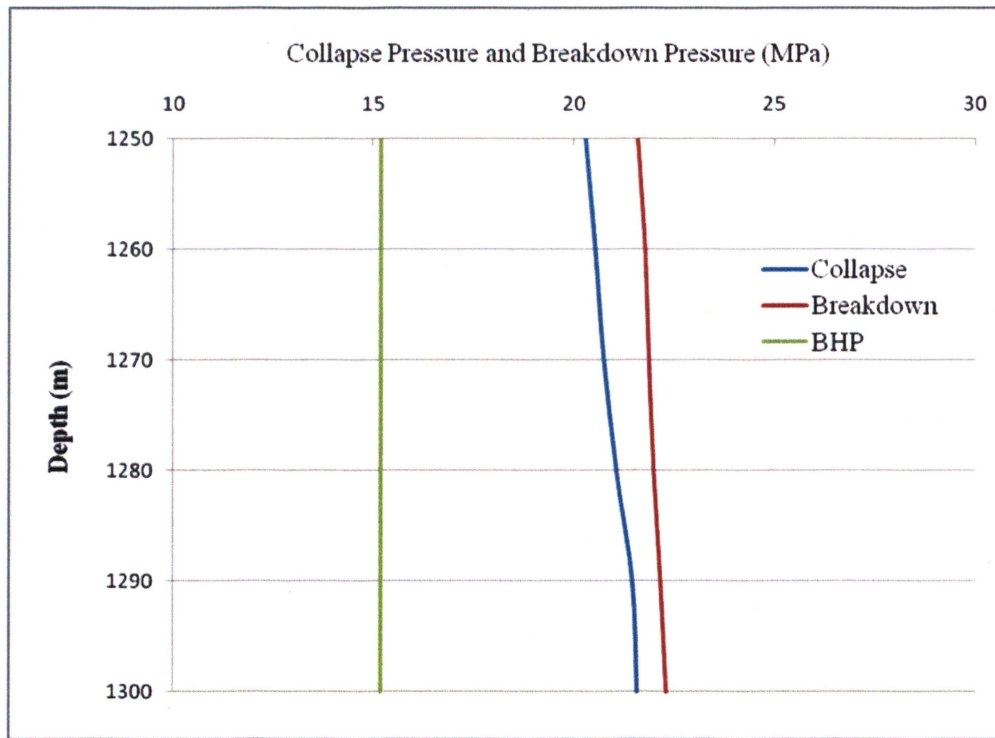


Figure 5.13. Collapse pressure and breakdown pressure due to CO₂ injection of the vertical well in the extensional case at day 1.

For the case that borehole pressure that sustains the wellbore is not considered, after 25 years of injection, the pore pressure will rise from 13.5 to 19.9 MPa, and then the in situ effective stresses will change in the reservoir. This will in turn cause higher hoop stress at 0 degrees and higher radial stress at 90 degrees of the wellbore wall, increasing the breakdown pressure and collapse pressure (Figure 5.14). The increase in the collapse pressure is greater than the breakdown pressure that leads to collapse pressure exceed the breakdown pressure such that no pressure can keep the wellbore from failure. The analysis is base on a non-completed well, and it shows the need to investigate short term and long term effects of the pore pressure to the wellbore integrity. The in-situ stress change due to the pore pressure causes increase in both breakdown and collapse pressures, and the increase in collapse pressure is much higher than the increase in the breakdown pressure that no interval for safe mud window exists. The wellbore must

have failed before the 25-year injection, and the critical injection time has to be further studied.

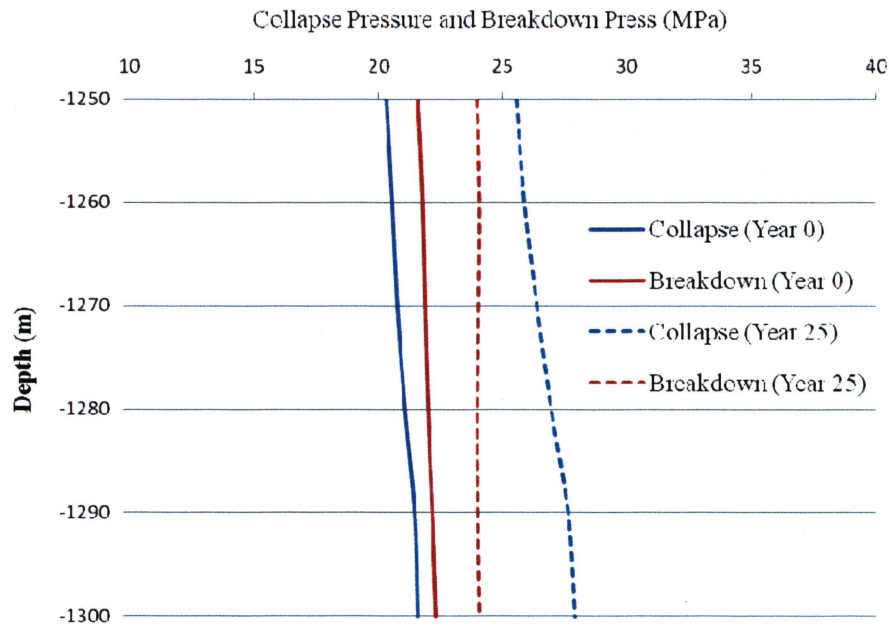


Figure 5.14. Collapse pressure and breakdown pressure due to CO₂ injection of the vertical well in the extensional case after 25 years.

5.6. OUTLOOK

In this study, only vertical wells and deviated wells of 45 and 90-degrees are studied. More comprehensive studies of wellbore stability in the generic reservoir can be further studied by utilizing the 3-D wellbore model for deviated wells in varied azimuths and inclined angles for the placement of the wellbore. Then suggestions for the optimal well placement in a generic anticline reservoir, i.e. trajectories and locations at the anticline structure to drill through (Figure 5.15), under different stress regimes can be made to minimize drilling-induced failures.

Due to the complexity of the modeling of a completed well, the wellbore integrity for CO₂ sequestration is investigated in an openhole section. This is because the homogeneous elastic model for validating the mesh optimization of the numerical model can only be applied for an openhole well scenario. Future works comprise modeling a

completed well with composite materials (casing and cement), cement failure mechanism and an appropriate interface debonding mechanism and applying such models for the evaluation of the risks of CO₂ leakage from the well. With the coupling module linking geomechanical and reservoir simulations, the influences of CO₂ storage factors such as injection rate, production rate, and storage time and the in-situ stresses and pore pressure changes from the CO₂ storage to the wellbore integrity can be analyzed in more detail.

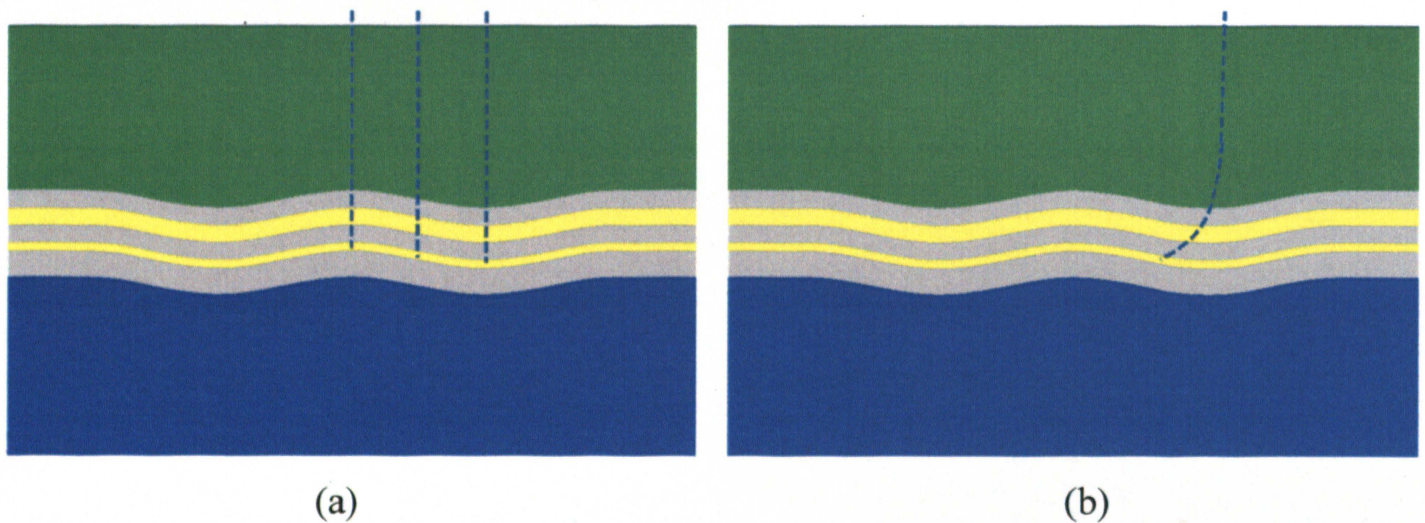


Figure 5.15. Evaluation of optimal wellbore path based on (a) locations of the anticline and (b) wellbore trajectories.

6. CONCLUSIONS

The use of finite element analysis in geomechanics provides an excellent tool for complex problems where analytical solutions do not exist, such as composite well completion systems necessary for well integrity analysis after CO₂ injection. The majority of numerical wellbore modeling studies rarely consider the influences of the way a model is discretized and the subsequent results deviated from the governing equation are often neglected. Since the wellbore integrity analysis relies on accuracy representation of state of stress at borehole wall, this study shows the inaccuracy from the numerical method may lead to a false interpretation of wellbore integrity. For the case of wellbore stress analyses the accuracy of the numerical results at the borehole wall and in its direct vicinity ensures the applicability of these results to wellbore stability, wellbore design, and cementing analyses, as well as hydraulic fracturing processes.

The present study shows that boundary conditions and meshing parameters, i.e. model size, element type and mesh density in the near-wellbore region, have a significant influence on the accuracy of results and if not appropriately chosen, the effective stresses in the near-wellbore region show significant errors (as high as 11 MPa) when compared to the analytical solution. This misfit shows the inherent need to conduct a mesh optimization for numerical wellbore stress analyses to minimize the errors. For 2-D wellbore stress analyses, displacement boundary conditions provide the best fit to the analytical solution for both the near-wellbore region and the far-field. The use of 2nd order quadrilateral elements and a relatively fine mesh in the near-wellbore region are of first priority to obtain accurate results. Further, the overall model size has to be chosen carefully.

With the meshing guideline presented in this study, a good match to the analytical solution throughout the model can be obtained and the error at the borehole wall and in the near-wellbore region can be minimized. It is expected that this general modeling technique also applies to more complex models. If discretization parameters are not optimized, the modeled results are of question and the subsequent analysis should not be relied on. Although the optimized mesh will significantly increase the computational processing time, the accuracy of the numerical should not be sacrificed.

This conclusion becomes evident for the cases of exemplary wellbore stability analysis in this study. Predicted safe mud weight windows from a non-optimized model for three different stress regimes show differences of up to -0.24 s.g. or 2.6 ppg compared to the analytical solution. For the cases presented this may specifically lead to a significant misinterpretation of the minimum usable mud weight and borehole collapse may result.

For the case of an exemplary generic anticline structure wellbore integrity analysis is studied for a drilling stage and a subsequent CO₂ injection stage. A wider mud weight window will give more options for the design of well trajectory, casing, shoe settlement, mud fluid, and also the wellbore stability; whereas a narrow mud weight window may require additional operations, for example, reducing penetration rates or setting of intermediate casing strings or drilling liners, which can greatly increase the total cost of the well. In summary, in an anticline structure, vertical drilling through the limb under the extensional stress regime shows favorable stability conditions because of wider mud weight window than at the crest or at the syncline. With a wider window, total depth can be reached with fewer casing strings. Inclined wellbores provides solutions for wellbore stability in the case that vertical well cannot be drilled in the strike-slip and compressional stress cases. This study only consists of vertical wells, 45°-inclined wells, and horizontal wells for the generic reservoir cases. Future study may continue to focus on the optimal trajectory of the wellbore placement.

Due to the limitation of the elastic model in the present study, the wellbore integrity of CO₂ injection is not practically analyzed in a completed well. A completed well model may consist of formation, cementing and casing, and the mechanism of the interfaces between the formation and cementing as well as casing and cementing. Since no analytical solution is available for the composite completed wellbore due to the complexity of the material heterogeneity, interface mechanism, failure mechanism, a geomechanical model utilizing FE 3-D wellbore is required for the evaluation of the risk of CO₂ leakage, and the coupling module helps identify the time of failure initiation and then a readjustment of the injection rate has to be undertaken.

The failure mechanism in a completed well is more complicated and the modeling procedure should be properly planned. Several factors have to be considered

for failure: pore pressure increase due to injection, corrosive CO₂ that can change the material properties and degrade the material strength, temperature effects, micro-fractures propagation in the cement, and debonding in the cement-formation and cement-casing interfaces. The numerical results should be carefully verified with field data or experiment data before being applied in the wellbore integrity analysis, to avoid errors resulting from the modeling such as presented in this study which shows erroneous leads to false conclusions in wellbore integrity analyses.

APPENDIX

Table A1. Model settings of the reservoir model.

Layer Name (Top to Bottom)	Material Name
Overburden	Overburden; 950m
Shale1	Shale; 100m
Sandstone 1	Sand; 100m
Cap Rock	Shale; 100m
Reservoir	Sand; 50m
Shale 3	Shale; 150m
Basement	Basement; 1050m

Material Name	Material Property
Overburden	Density: 2.6E3 kg/m ³ Young's Modulus: 15 GPa Hydraulic Conductivity: 1.0E-6 m/s
Shale	Density: 2.5E3 kg/m ³ Young's Modulus: 15 GPa Hydraulic Conductivity: 3.227E-18 m/s
Sand	Density: 2.6E3 kg/m ³ Young's Modulus: 20 GPa Hydraulic Conductivity: 1.6135E-6 m/s
Basement	Density: 2.65E3 kg/m ³ Young's Modulus: 15 GPa Hydraulic Conductivity: 1.0E-6 m/s

Rock Strength of the Reservoir Layer	
Cohesion	12 MPa
Friction Angle	42°
Tensile Strength	5 MPa

BIBLIOGRAPHY

- [1] Kirsch, G. 1898. Die Theorie der Elastizität und die Bedürfnisse der Festigkeitslehre. Zeitschrift des Vereines Deutscher Ingenieure. 42: 797.
- [2] Bradley, W.B. 1979. Failure of inclined boreholes. J. Energy Resour. Technol. 101: 232-239.
- [3] Zhang, J., W.B. Standifird, K. Adesina, and G. Keaney. 2006. Wellbore stability with consideration of pore pressure and drilling fluid interactions. In the 41st U.S. Symposium on Rock Mechanics, Golden, CO, 17 - 21 June, 2006.
- [4] Gentzis, T., D. Nathan, and R.J. Chalaturnyk. 2009. A method to predict geomechanical properties and model well stability in horizontal boreholes. International Journal of Coal. 78: 149-160.
- [5] Cheng, H. and M.B. Dusseault. 1993. Development and application of a fully-coupled two-dimensional finite element approach to deformation and pressure diffusion around a borehole. Journal of Canadian Petroleum Technology. 32: 28-38.
- [6] Zervos, A., P. Papanastasiou, and J. Cook. 1998. Elastoplastic finite element analysis of inclined wellbores. In SPE/ISRM Rock Mechanics in Petroleum Engineering, Trondheim, Norway. 8 - 10 July 1998. SPE/ISRM 47322.
- [7] Zhang, J., M. Bai, and J.-C. Roegiers. 2003. Dual-porosity poroelastic analyses of wellbore stability. International Journal of Rock Mechanics and Mining Sciences. 40: 473-483.
- [8] Zienkiewicz, O.C., R.L. Taylor, and J.Z. Zhu. The finite element method: its basis and fundamentals. 6th ed. Butterworth-Heinemann.
- [9] Rutqvist, J., P. Digby, and O. Stephansson. 1989. Simulation of borehole breakouts with a damage material model. In ISRM International Symposium, Pau, France, 30 August - 2 September 1989.
- [10] Zahn, M.N., L.C. Coelho, L. Landau, and J.L.D. Alves. 2010. Numerical study on wellbore stability analysis considering volumetric failure. Mecánica Computacional. 29: 8837-8858.
- [11] Grabinsky, M.W., R. Wilson, and A. Zougas. 1995. Practical meshing considerations for finite element analysis of rock engineering problems. In 8th ISRM Congress, Tokyo, Japan, 25-29 September 1995. SPE 8CONGRESS-1995-266.

- [12] Turon, A., C.G. Davila, P.P. Camanho, and J. Costa. 2007. An engineering solution for mesh size effects in the simulation of delamination using cohesive zone models. *Journal of Engineering Fracture Mechanics*. 74, 1665-1682.
- [13] Nipp, H.-K, E.G. McNulty. 1987. Effects of mesh size and boundary conditions on creep analysis of rock salt. In *The 28th U.S. Symposium on Rock Mechanics*, Tucson, AZ, 29 June - 1 July 1987.
- [14] Davis, R.O. and A.P.S. Selvadurai, 1996. *Elasticity and Geomechanics*. Cambridge University Press, Cambridge.
- [15] Ranalli, G. 2005. *Rheology of the earth*, Chapman & Hall, London.
- [16] Jaeger, J.C., N.G.W. Cook, and R.W. Zimmerman, 2007. *Fundamental of Rock Mechanics*, 4th edition, Blackwell Publishing.
- [17] Pollar, D.D. and R.C. Fletcher. 2005. *Fundamentals of Structural Geology*. Cambridge University Press, Cambridge.
- [18] McLean, M.R. and M.A. Addis. 1990. Wellbore stability: the effect of strength criteria on mud weight recommendations. In *SPE Annual Technical Conference and Exhibition*, New Orleans, LA, 23-26 September 1990. SPE 20405-MS.
- [19] Zhang, L., P. Cao, and K.C. Radha. 2010. Evaluation of rock strength criteria for wellbore stability analysis. *International Journal of Rock Mechanics and Mining Sciences*. 47: 1304-1316.
- [20] Ewy, R.T. 1999. Wellbore-stability prediction by use of a modified Lade criterion. *SPE Drilling & Completion*. 14: 85-91.
- [21] Tran, M. H. and Y.N. Abousleiman. 2010. The impacts of failure criteria and geological stress states on the sensitivity of parameters in wellbore stability analysis. In *44th U.S. Rock Mechanics Symposium and 5th U.S.-Canada Rock Mechanics Symposium*, Salt Lake City, UT, June 27 - 30, 2010.
- [22] Nawrocki, P.A. 2010. Critical wellbore pressures using different rock failure criteria. In *International Symposium - 6th Asian Rock Mechanics Symposium*, New Delhi, India, 23-27 October 2010.
- [23] Coulomb, C.A. 1776. Essai sur une application des regles des maximis et minimis a quelques problemes de statique relatifs, a la architecture. *Mem. Acad. Roy. Div. Sav.* 7: 343-387.
- [24] Saouma, V.E. 2010. *Continuum Mechanics and Elements of Elasticity/Structural Mechanics*. Department of Civil Environment and Architectural Engineering at University of Colorado at Boulder.

- [25] Felippa, C.A. 2002. Introduction to Finite Element Methods. Department of Aerospace Engineering Sciences at University of Colorado at Boulder.[14]Pollar, D.D. and R.C. Fletcher. 2005. Fundamentals of Structural Geology. Cambridge University Press.
- [26] Mitchell, S.A. 1997. Choosing corners of rectangles for mapped meshing. In Proceedings of the thirteenth annual symposium on Computational geometry, New York, NY, 1997. 87-93.
- [27] Knupp, P.M. 2007. Remarks on mesh quality. In 45th AIAA Aerospace Sciences Meeting and Exhibit, Reno, NV, 7-10 January, 2007.
- [28] Chen, G., M.E. Chenevert, M.M. Sharma, and M. Yu. 2003. A study of wellbore stability in shales including poroelastic, chemical, and thermal effects. Journal of Petroleum Science and Engineering. 38: 167-176.
- [29] Peska, P. and M.D. Zoback. 1995. Compressive and tensile failure of inclined wellbores and determination of in situ stress and rock strength. J. Geophys. Res 100: 12791-12811.
- [30] Gray, K.E., E. Podnos, and E. Becker. 2009. Finite-Element Studies of Near-Wellbore Region During Cementing Operations: Part I. SPE Drilling & Completion. 24: 127-136.
- [31] Freitag, L., M. Jones, and P. Plassman. 1995. An Efficient Parallel Algorithm for Mesh Smoothing. In Proceedings of the Fourth International Meshing Round Table, 1995. 47-58.
- [32] Zavattieri, P. 1996. Optimization Strategies in Unstructured Mesh Generation. International Journal for Numerical Methods in Engineering. 39: 2055-2071.
- [33] Knupp, P.M. 2000. Achieving finite element mesh quality via optimization of the Jacobian matrix norm and associated quantities. Part I- A framework for surface mesh optimization. Int. J. Numer. Meth. Engng. 48: 401-420.
- [34] ABAQUS Analysis User's Manual V6.10. Chapters 4.1.3 and 25.1.3. ABAQUS, Inc. Dassault Systèmes.
- [35] Al-Ajmi, A.M., U. Sultan Qaboos, and R.W. Zimmerman. 2006. Stability Analysis of Deviated Boreholes Using the Mogi-Coulomb Failure Criterion, With Applications to Some Oil and Gas Reservoirs. In IADC/SPE Asia Pacific Drilling Technology Conference and Exhibition, Bangkok, Thailand, 13-15 November 2006. SPE 104035-MS.

- [36] Tirado, G.R., C.M.P. Lupo, J.C. Beltran, H. Duno, C.O. Iturrios, J.F. Gallo, T. Hernandez, and M. Centeno. MPD makes possible to drill and trip out of the hole in a gas well with a combination of a narrow mud weight window and a serious ballooning effect. In IADC/SPE Managed Pressure Drilling and Underbalanced Operations Conference & Exhibition, 5-6 April 2011, Denver, Colorado. SPE 143104-MS.
- [37] IPCC Special Report on Carbon Dioxide Capture and Storage. 2005. Intergovernmental Panel on Climate Change. Cambridge University Press, Cambridge, United Kingdom and New York, NY, USA.
- [38] Eckert, A and M. Paradeis. 2010. Geomechanical risks associated with CO₂ sequestration in generic reservoir settings. In 2010 Geological Society of America Annual Meeting, Denver, Colorado, 31 October – 3 November, 2010.
- [39] Amirlatifi, A, A. Eckert, R. Nygaard, and B. Bai. 2011. Coupled reservoir and geomechanical modeling to predict CO₂ induced caprock failure. In 10th Annual Conference on Carbon Capture & Sequestration, Pittsburgh, Pennsylvania, 2-5 May, 2011.

VITA

Ming-Yen Lee was born and raised in Taipei, Taiwan. He earned his Bachelor and Master's degrees in Mechanical Engineering in 1997 and 2002, respectively, from National Taiwan University. After graduation, he pursued his career in patent law, working as a patent associate at intellectual property law firms in Taipei, Taiwan for five years.

In August 2009, he attended Missouri University of Science and Technology in Rolla, Missouri for his graduate studies in petroleum engineering. Later, he held positions of graduate research assistant and graduate teaching assistant in the Department of Geological Science and Engineering.